1700 Chem. Rev. **2006,** *106,* 1700−1719

Characterization of the Dynamics of Biomacromolecules Using Rotating-Frame Spin Relaxation NMR Spectroscopy

Arthur G. Palmer, III* and Francesca Massi

Department of Biochemistry and Molecular Biophysics, Columbia University, 630 West 168th Street, New York, New York 10032

Received May 16, 2005

Contents

1. Introduction 1700
2. Theory 1701
   2.1. Two-, Three-, and *N*-Site Chemical Exchange 1701
   2.2. Rotating-Frame Relaxation 1702
3. Experimental Methods 1707
   3.1. Pulse Sequences for ^{15}N $R_{1\rho}$ Measurements 1707
   3.2. Pulse Sequences for ^{1}H and ^{13}C $R_{1\rho}$ Measurements 1709
   3.3. Experimental Considerations for $R_{1\rho}$ Relaxation 1711
      3.3.1. Temperature Control 1711
      3.3.2. Water Suppression 1711
      3.3.3. Calibration of Radio Frequency Fields and Validation of Alignment 1712
4. Applications 1712
   4.1. Protein Folding 1714
   4.2. Ligand Binding 1716
   4.3. Catalysis 1717
5. Conclusions 1718
6. Acknowledgments 1718
7. References 1718

1. Introduction

Time-dependent dynamical properties of molecules can be quantified with atomic resolution by using solution-state NMR spectroscopy. A variety of NMR observables, including scalar and dipolar coupling constants, amide−solvent proton exchange rates, and spin relaxation rate constants, depend on changes in molecular structure or chemical state through well-established theoretical relationships.[1] Over the past decade, solution-state NMR techniques for measuring spin relaxation rate constants have proven particularly powerful for investigations of picosecond to nanosecond and microsecond to millisecond time scale dynamical processes in proteins and other biomacromolecules.[2−4]

Solution-state NMR spin relaxation methods for characterizing microsecond to second time scale kinetic processes and conformational dynamics have been extensively reviewed.[2,5,6] Methods in common use include *zz*-exchange techniques, line shape analysis, Carr−Purcell−Meiboom−Gill (CPMG) relaxation dispersion, and $R_{1\rho}$ relaxation dispersion. The choice of which technique to apply is based on the time scale of the kinetic or conformational dynamical process. CPMG and $R_{1\rho}$ experiments have been the predominant choices for studying exchange processes that occur in the microsecond to millisecond time scale and that have highly skewed site populations.[2] The accessible range of effective magnetic field strengths determines the time scale of the process that can be studied by CPMG and $R_{1\rho}$ techniques.[5] The effective field strengths typically employed in CPMG relaxation experiments are on the order of 25−500 Hz; consequently, CPMG

Arthur G. Palmer, III, is Professor of Biochemistry and Molecular Biophysics at Columbia University. He received his Ph.D. in Chemistry with Nancy L. Thompson from the University of North Carolina at Chapel Hill. He was a National Science Foundation Postdoctoral Fellow with Peter E. Wright at the Scripps Research Institute. His research interests are NMR spin relaxation and molecular motions in biological macromolecules.

Francesca Massi is an Associate Research Scientist in the Department of Biochemistry and Molecular Biophysics at Columbia University. She received her Ph.D. in Chemistry with John E. Straub from Boston University and was a postdoctoral fellow with Arthur G. Palmer at Columbia University. Her research interests are protein function and dynamics studied with NMR spin relaxation experiments and computer simulations.

---

* To whom correspondence should be addressed. Telephone: (212) 305-8675. Fax: (212) 305-6949. E-mail: agp6@columbia.edu.

10.1021/cr0404287 CCC: $59.00

experiments are most often used to characterize slower, millisecond time scale chemical exchange processes. The effective field strengths typically employed in $R_{1\rho}$ relaxation experiments are of the order of 1−6 kHz, although weaker fields can be utilized to provide overlap with the CPMG experiment;[7,8] consequently, $R_{1\rho}$ experiments are most often used for faster microsecond time scale chemical exchange processes. Although these techniques have been in use for many years, a number of advances in theoretical descriptions, experimental methods, and applications of $R_{1\rho}$ relaxation have been developed recently.[7−17] The purpose of this Review is to provide a comprehensive description of theory, techniques, and applications of $R_{1\rho}$ measurements to biomacromolecules.

2. Theory

Chemical exchange is a ubiquitous phenomenon in NMR spectroscopy that mediates population transfer among longitudinal spin operators, affects line shapes in free-precession NMR spectra, and, of particular interest in the following, contributes to relaxation of magnetization spin-locked in the rotating frame of reference.

2.1. Two-, Three-, and *N*-Site Chemical Exchange

Chemical exchange refers to one or more kinetic processes, which may be intra- or intermolecular, that transfer nuclear spins between environments with different local magnetic fields. The most general kinetic scheme is

$$A_1 \underset{k_{21}}{\overset{k_{12}}{\rightleftharpoons}} A_2;\quad A_1 \underset{k_{31}}{\overset{k_{13}}{\rightleftharpoons}} A_3;\quad \ldots;\quad A_i \underset{k_{ji}}{\overset{k_{ij}}{\rightleftharpoons}} A_j;\quad \ldots;$$
$$A_{(N-1)} \underset{k_{N(N-1)}}{\overset{k_{(N-1)N}}{\rightleftharpoons}} A_N \quad (1)$$

in which spins in N environments mutually exchange with rate constants k_{ij} for the exchange from site i to site j. If any of the kinetic reactions are not unimolecular, then the kinetic rate constants in eq 1 are defined to be the appropriate pseudo-first-order rate constants.[5] The equilibrium site populations are given by the solution to

$$\mathbf{KP} = 0 \quad (2)$$

in which $\mathbf{P} = [p_1, p_2, ..., p_N]^{\mathrm{T}}$, p_i is the equilibrium population of the ith site, the matrix of kinetic rate constants is

$$\mathbf{K} = \begin{bmatrix} -s_1 & k_{21} & \cdots & k_{N1} \\ k_{12} & -s_2 & \cdots & k_{N2} \\ \vdots & \vdots & \ddots & \vdots \\ k_{1N} & k_{2N} & \cdots & -s_N \end{bmatrix} \quad (3)$$

and the diagonal elements s_i are given by

$$s_i = \sum_{\substack{j=1 \\ i\neq j}}^{N} k_{ij} \quad (4)$$

A nuclear spin in the ith site or environment is characterized by the resonance offset frequency, Ω_i, and the intrinsic relaxation rate constants, R_{1i} and R_{2i}. The intrinsic relaxation rate constants result from dipole−dipole, chemical shift anisotropy, and quadrupolar interactions in solution. These interactions are modulated stochastically by overall rotational tumbling on a time scale $\tau_m \ll 1/k_{ij}$ for all i and j. Consequently, the effects of rotational tumbling and chemical exchange are uncorrelated.[1,18,19] Evolution of the density operator for a spin system subject to chemical exchange is described by the Bloch−McConnell or Stochastic Liouville equations (SLE).[12,20,21] For a single uncoupled spin in a Cartesian basis, the Bloch−McConnell equations and SLE are identical:

$$\frac{\mathrm{d}\mathbf{M}(t)}{\mathrm{d}t} = (\mathbf{L} + \Gamma)\mathbf{M}(t) \quad (5)$$

in which

$$\mathbf{M}(t) = \begin{bmatrix} \mathbf{M}_1(t) \\ \mathbf{M}_2(t) \\ \vdots \\ \mathbf{M}_N(t) \end{bmatrix} \quad (6)$$

$$\mathbf{L} = \begin{bmatrix} \mathbf{L}_1 & & & 0 \\ & \mathbf{L}_2 & & \\ & & \ddots & \\ 0 & & & \mathbf{L}_N \end{bmatrix} \quad (7)$$

$$\boldsymbol{\Gamma} = \mathbf{K} \otimes \mathbf{1}_s \quad (8)$$

$\mathbf{M}_i(t) = [M_{xi}(t), M_{yi}(t), M_{zi}(t)]^{\mathrm{T}}$ is the Cartesian magnetization vector for spins in the ith site, which is understood to represent the deviation of the magnetization from Boltzman equilibrium;

$$\mathbf{L}_i = \begin{bmatrix} -R_{2i} & -\Omega_i & 0 \\ \Omega_i & -R_{2i} & -\omega_1 \\ 0 & \omega_1 & -R_{1i} \end{bmatrix} \quad (9)$$

ω_1 is the amplitude of the spin-locking radio frequency (rf) field, assumed without loss of generality to be applied with x-phase; and $\mathbf{1}_s$ is the 3 × 3 identity matrix in the spin space.

If the differences between intrinsic relaxation rate constants for the N sites are small compared to the kinetic rate constants, that is $|R_{1i} - R_{1j}| \ll k_{ij}$ and $|R_{2i} - R_{2j}| \ll k_{ij}$ for all i and j, then the site-specific intrinsic relaxation rate constants can be replaced by the population-average values:

$$\bar{R}_j = \sum_{i=1}^{N} p_i R_{ji}\ (j = 1, 2) \quad (10)$$

This assumption is valid for the situations normally investigated by $R_{1\rho}$ methods and will be made in the following; violations of this assumption have been discussed.[22]

The general scheme has a number of illustrative special cases. The starlike topology is

$$A_1 \underset{k_{21}}{\overset{k_{12}}{\rightleftharpoons}} A_2;\quad A_1 \underset{k_{31}}{\overset{k_{13}}{\rightleftharpoons}} A_3;\quad \ldots;\quad A_1 \underset{k_{N1}}{\overset{k_{1N}}{\rightleftharpoons}} A_N \quad (11)$$

In this model, sites 2, 3, ..., N only exchange with site 1 and not with each other. When $N = 3$, the starlike topology reduces to a linear three-site exchange model:

$$A_2 \underset{k_{12}}{\overset{k_{21}}{\rightleftharpoons}} A_1 \underset{k_{31}}{\overset{k_{13}}{\rightleftharpoons}} A_3 \quad (12)$$

A second linear three-site exchange model can be formulated in which site 1 is located at the end of the linear chain,

$$A_1 \underset{k_{21}}{\overset{k_{12}}{\rightleftarrows}} A_2 \underset{k_{32}}{\overset{k_{23}}{\rightleftarrows}} A_3 \tag{13}$$

rather than being central, as in the starlike topology. The two-site exchange model is the simplest possible case and the one most commonly applied:

$$A_1 \underset{k_{21}}{\overset{k_{12}}{\rightleftarrows}} A_2 \tag{14}$$

Finally, if sites 2, 3, ..., N exchange sufficiently rapidly with each other, relative to the exchange with site 1, then the general N-site scheme is reduced to an effective two-site system:

$$A_1 \underset{k'_{21}}{\overset{k'_{12}}{\rightleftarrows}} A'_2 \tag{15}$$

The properties of the effective site, A'_2, are given by the following:[11]

$$k'_{12} = \sum_{i=2}^{N} k_{1i} \tag{16}$$

$$k'_{21} = \sum_{i=2}^{N} \alpha_i k_{i1} \tag{17}$$

$$\mathbf{L}'_2 = \sum_{i=2}^{N} \alpha_i \mathbf{L}_i \tag{18}$$

in which

$$\alpha_i = p_i / \sum_{j=2}^{N} p_j = p_i/(1 - p_1) \tag{19}$$

2.2. Rotating-Frame Relaxation

By analogy to the laboratory-frame Bloch equations, $R_{1\rho}$ is the relaxation rate constant for magnetization locked along the direction of the effective field in the rotating frame, and $R_{2\rho}$ is the relaxation rate constant for magnetization orthogonal to the direction of the effective field in the rotating frame. The rotating-frame relaxation rate constants contain contributions from $\bar{R}_1$ and $\bar{R}_2$ that result from transformation from the laboratory frame to the rotating frame. This dependence can be removed by measuring $\bar{R}_1$ and $\bar{R}_2$ independently. For example, an effective transverse relaxation rate constant R_2 is defined as

$$R_2 = R_{1\rho}/\sin^2\theta - \bar{R}_1/\tan^2\theta \tag{20}$$

and the pure exchange contribution to $R_{1\rho}$ is given by[23]

$$R_{\mathrm{ex}} = R_{1\rho}/\sin^2\theta - \bar{R}_2 - \bar{R}_1/\tan^2\theta \tag{21}$$

in which the tilt angle in the rotating frame is[23]

$$\tan\theta = \frac{\omega_1}{\bar{\Omega}} \tag{22}$$

the average resonance offset is[23]

$$\bar{\Omega} = \sum_{i=1}^{N} p_i \Omega_i \tag{23}$$

and the average effective field in the rotating frame is[23]

$$\omega_{\mathrm{e}} = (\bar{\Omega}^2 + \omega_1{}^2)^{1/2} \tag{24}$$

A similar expression can be derived for $R_{2\rho}$.[12] The geometrical relationship between the laboratory and tilted reference frames is illustrated in Figure 1.

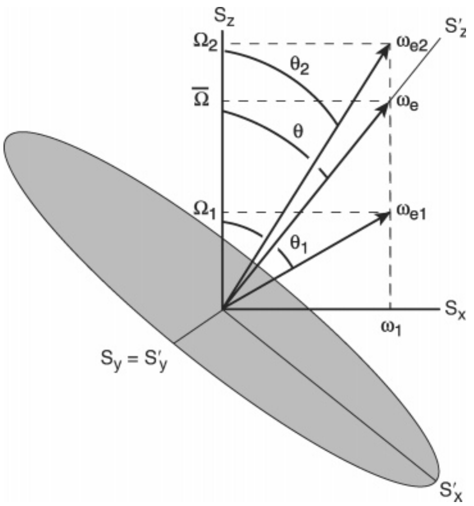

Figure 1. Geometric representation of the laboratory and tilted reference frames. The relative orientation of the laboratory frame (S_x, S_y, S_z) and of the tilted rotating frame (S'_x,S'_y,S'_z) is given by the tilt angle θ. The tilted rotating frame is defined for each spin. The orientation of S'_z is parallel to the average effective field, ω_{e}. The orientations of the effective fields of the two exchanging sites $\omega_{\mathrm{e}1}$ and $\omega_{\mathrm{e}2}$ are given by θ_1 and θ_2, respectively.

Theoretical expressions for rotating-frame relaxation rate constants have been derived principally by two approaches. When exchange is sufficiently fast, the Redfield approach is valid, as introduced for exchange processes by Wennerström.[24] In the fast exchange limit, both $R_{1\rho}$ and $R_{2\rho}$ can be calculated by this approach. For all exchange regimes, $R_{1\rho}$ can be approximated from the Bloch−McConnell equation or SLE, either in a time-domain or Laplace-domain formalism, as introduced by Trott, Abergel, and Palmer.[10] The expressions for $R_{1\rho}$ derived below are summarized in Table 1. The approaches utilized for calculating rotating-frame relaxation rate constants also can be used to obtain expressions for laboratory-frame free-precession transverse relaxation rate constants for spins subject to chemical exchange broadening.[11,25]

In the fast exchange regime, a general solution for N-site exchange is[12]

$$R_{1\rho} = \bar{R}_1 \cos^2\theta + \bar{R}_2 \sin^2\theta + \sin^2\theta \sum_{i=2}^{N} \frac{|\langle u_1|\Omega|u_i\rangle|^2 \lambda_i}{\lambda_i{}^2 + \omega_{\mathrm{e}}{}^2} \tag{25}$$

in which λ_i and u_i are the ith eigenvalue and eigenvector, respectively, of the symmetrized matrix $\mathbf{S}^{-1}\mathbf{\Gamma}\mathbf{S}$, $\mathbf{S}$ is a diagonal matrix with elements $S_{ij} = \delta_{ij}\, p_i^{1/2}$, and $\mathbf{\Omega}$ is a diagonal matrix with elements $\Omega_{ij} = \delta_{ij}\Omega_i$. For the linear

Table 1. Summary of Expressions for $R_{1\rho}$

site	chemical shift time scale	model assumption	eq
2-site	fast exchange		30
2-site	general	single-exponential decay	31
2-site	general	asymmetric populations	33
2-site	general	Laguerre approximation	34
2-site	general	equal populations or average resonance frequency	35
3-site star	fast exchange		26−27
3-site	fast exchange	independent processes	29
N-site	fast exchange		25
N-site	general	single dominant site population	36
N-site star	general	single dominant site population	40
N-site	slow exchange between minor sites	single dominant site population	41
N-site	fast exchange between minor sites	single dominant site population	42

three-site system given by eq 12, $R_{1\rho}$ is given by eq 25 with

$$|\langle u_1|\Omega|u_2\rangle|^2 = (-\lambda_3\alpha_1 + \alpha_2)/Z$$

$$|\langle u_1|\Omega|u_3\rangle|^2 = (-\lambda_2\alpha_1 + \alpha_2)/Z$$

$$\lambda_2 = (k_{ex} + Z)/2$$

$$\lambda_3 = (k_{ex} - Z)/2 \qquad (26)$$

in which

$$k_{ex} = k_{12} + k_{21} + k_{13} + k_{31}$$

$$Z = (k_{ex}^2 - 4B)^{1/2}$$

$$B = k_{21}k_{31} + k_{12}k_{31} + k_{21}k_{13}$$

$$\alpha_1 = p_1p_2\Delta\omega_{21}^2 + p_2p_3\Delta\omega_{32}^2 + p_1p_3\Delta\omega_{31}^2 \qquad (27)$$

$$\alpha_2 = p_1[k_{12}\Delta\omega_{21}^2 + k_{13}\Delta\omega_{31}^2]$$

$$p_1 = k_{21}k_{31}/B$$

$$p_2 = k_{12}k_{31}/B$$

$$p_3 = k_{21}k_{13}/B$$

and $\Delta\omega_{ij} = \Omega_i - \Omega_j$. If the rate constants for the two kinetic steps differ substantially, such that

$$|(k_{13} + k_{31}) - (k_{12} + k_{21})| \gg 2(k_{12}k_{13})^{1/2} \qquad (28)$$

then the two steps are independent of each other and eq 25 simplifies to

$$R_{1\rho} = \bar{R}_1 \cos^2\theta + \bar{R}_2 \sin^2\theta + \sin^2\theta \sum_{i=2}^{3} \frac{p_i(1-p_i)\Delta\omega_{i1}^2(k_{1i} + k_{i1})}{(k_{1i} + k_{i1})^2 + \omega_e^2} \qquad (29)$$

Results for the linear three-site system given by eq 13 are obtained by interchanging the site 1 and 2 indices in eqs 26−29. The general fast exchange solution reduces for the two-site system to

$$R_{1\rho} = \bar{R}_1 \cos^2\theta + \bar{R}_2 \sin^2\theta + \sin^2\theta \frac{p_1p_2\Delta\omega_{21}^2k_{ex}}{k_{ex}^2 + \omega_e^2} \qquad (30)$$

in which $k_{ex} = k_{12} + k_{21}$. The quantity $\phi_{ex} = p_1p_2\Delta\omega_{21}^2$ frequently is defined as one of the independent variables in eq 30.

General solutions for $R_{1\rho}$, valid for all time scales, can be obtained approximately for the two-site model when $p_1 > p_2$ (typically $p_1 > 0.7$) and for the *N*-site model when $p_1 \gg p_i$, for $i = 2, 3, ..., N$ (typically $p_1 > 0.9$). Approximate solutions are determined from the Bloch−McConnell equation or the SLE as the dominant eigenvalue in the time-domain or long-time limit of the resolvent in the Laplace domain.[12] For two-site exchange, the resulting expression for $R_{1\rho}$, accurate whenever relaxation is dominated by a single-exponential decay, is given by

$$R_{1\rho} = \bar{R}_1 \cos^2\theta + \bar{R}_2 \sin^2\theta + \frac{1}{\gamma} \times \frac{\sin^2\hat{\theta}\, p_1p_2\Delta\omega_{21}^2k_{ex}}{\hat{\omega}_{e1}^2\hat{\omega}_{e2}^2/\hat{\omega}_e^2 + k_{ex}^2 - 2\sin^2\hat{\theta}\, p_1p_2\Delta\omega_{21}^2 + (1-\gamma)\omega_1^2} \qquad (31)$$

in which $\hat{\omega}_{ei} = (\Omega_i^2 + \gamma\omega_1^2)^{1/2}$, $\hat{\omega}_e = (\bar{\Omega}^2 + \gamma\omega_1^2)^{1/2}$, $\sin^2\hat{\theta} = \gamma\omega_1^2/\hat{\omega}_e^2$

$$\gamma = 1 + p_1p_2\Delta\omega_{21}^2(\sigma^2 + \omega_1^2 - k_{ex}^2)/(\sigma^2 + \omega_1^2 + k_{ex}^2)^2 \qquad (32)$$

and $\sigma = p_1\Omega_2 + p_2\Omega_1$. When $\gamma \rightarrow 1$, then $\hat{\theta} \rightarrow \bar{\theta}$, $\hat{\omega}_e \rightarrow \omega_e$, and $\hat{\omega}_{ei} \rightarrow \omega_{ei}$, in which the effective field in the rotating frame for spins in the *i*th site is given by $\omega_{ei} = (\Omega_i^2 + \omega_1^2)^{1/2}$. If the site populations are highly skewed ($p_1 \gg p_2$), then the simple, so-called "asymmetric populations", result is obtained:[9]

$$R_{1\rho} = \bar{R}_1 \cos^2\theta + \bar{R}_2 \sin^2\theta + \frac{\sin^2\theta\, p_1p_2\Delta\omega_{21}^2k_{ex}}{\Omega_2^2 + \omega_1^2 + k_{ex}^2} \qquad (33)$$

This expression has the same functional form as eq 30, except that the exchange contribution depends on the effective field for spins in the less-populated site 2, $\omega_{e2} = (\Omega_2^2 + \omega_1^2)^{1/2}$, rather than on the effective field for the averaged resonance position.

Conditions that define the fast exchange limit have been discussed by Abergel and Palmer and are more complex than those obtained for free-precession chemical exchange line broadening.[12] Comparison of eqs 30 and 31 shows, however, that the fast exchange limit is reached for asymmetric

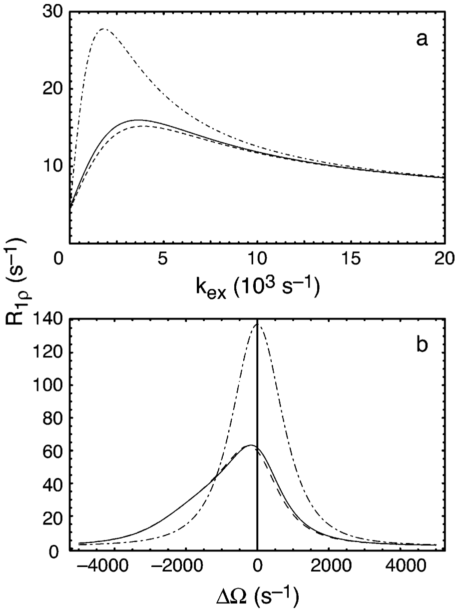

Figure 2. Comparison of fast and asymmetric two-site exchange expressions for $R_{1\rho}$. Shown are (—) the exact numerical eigenvalue, (- - -) the asymmetric population solution for $p_1 \gg p_2$ given by eq 33, and (— - —) the fast exchange limit solution given by eq 33. Calculations used $\bar{R}_1 = 1.5$ s^{-1}, $\bar{R}_2 = 11$ s^{-1}, $\Delta\omega_{21} = 2400$ s^{-1}, $p_1 = 0.95$, and $\omega_1 = 1000$ s^{-1}. In (a) $\bar{\Omega} = 1500$ s^{-1}. In (b) $k_{ex} = 1500$ s^{-1}. In (b) the abscissa shows $\Delta\Omega = \Omega - \omega_{rf}$.

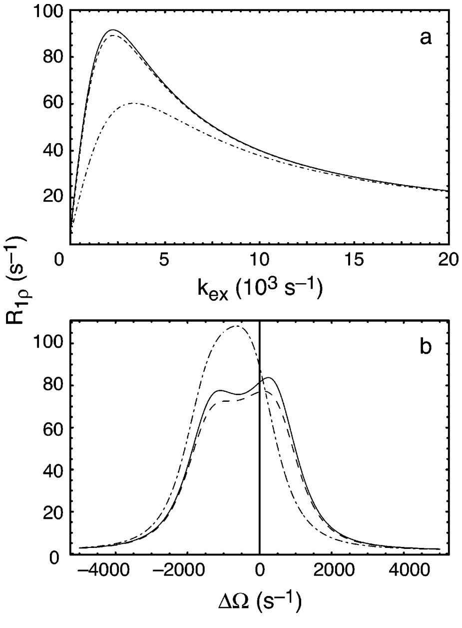

Figure 3. Comparison of asymmetric and general two-site exchange expressions for $R_{1\rho}$. Shown are (—) the exact numerical eigenvalue, (- - -) the general solution for $p_1 > p_2$ given by eq 31, and (— - —) the asymmetric population solution for $p_1 \gg p_2$ given by eq 33. Calculations used $\bar{R}_1 = 1.5$ s^{-1}, $\bar{R}_2 = 11$ s^{-1}, $\Delta\omega_{21} = 2400$ s^{-1}, $p_1 = 0.7$, and $\omega_1 = 1000$ s^{-1}. In (a) $\bar{\Omega} = 1500$ s^{-1}. In (b) $k_{ex} = 250$ s^{-1}. In (b) the abscissa shows $\Delta\Omega = \Omega - \omega_{rf}$.

populations if any one of the three following conditions are met: $|\bar{\Omega}| \gg |\Delta\omega_{21}|$, $\omega_1 \gg |\Delta\omega_{21}|$, or $k_{ex} \gg |\Delta\omega_{21}|$.

The accuracy of eqs 31 and 33 is illustrated in Figures 2 and 3. When $p_1 \gg p_2$, the asymmetric population result is highly accurate, but the fast exchange limit equation, eq 30, is accurate only for sufficiently large values of k_{ex}, as illustrated in Figure 2. When the site populations are not highly asymmetric, then the general expression, eq 31, is more accurate, as shown in Figure 3.

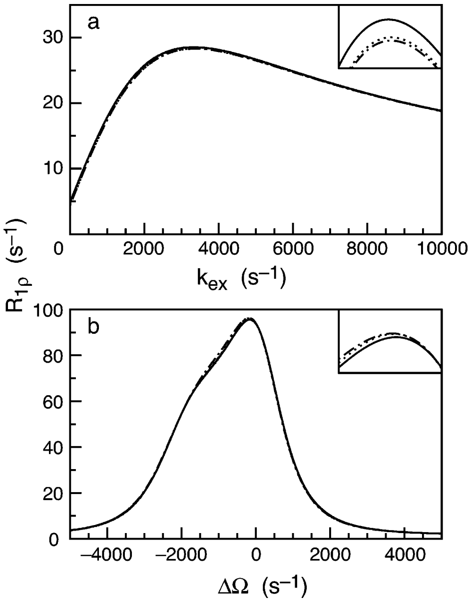

Figure 4. Exchange rate dependence of the $R_{1\rho}$ relaxation rate constant. Shown are (—) the exact numerical eigenvalue, (— - —) the general solution for $p_1 > p_2$ given by eq 31, and (•••) the solution given by the linearized Laguerre approximant, eq 34. Calculations used $\bar{R}_1 = 1.5$ s^{-1}, $\bar{R}_2 = 11$ s^{-1}, $\Delta\omega_{21} = 2400$ s^{-1}, $p_1 = 0.9$, and $\omega_1 = 1000$ s^{-1}. In (a) $\Delta\Omega = 1500$ s^{-1}; the inset shows the region of k_{ex} (2700, 4000), $R_{1\rho}$ (28, 28.7). In (b) $k_{ex} = 1000$ s^{-1}; the inset shows the region of $\Delta\Omega$ (−500, 100), $R_{1\rho}$ (90, 100). In (b) the abscissa shows $\Delta\Omega = \Omega - \omega_{rf}$.

Using Laguerre's method for polynomial root finding, Miloushev and Palmer derived a general formula for $R_{1\rho}$ relaxation for two-site chemical exchange as the root of a (p_1,q_1) Padé approximant[26]

$$R_{1\rho} = \bar{R}_1 \cos^2\theta + \bar{R}_2 \sin^2\theta + \frac{\sin^2\theta\, p_1 p_2 \Delta\omega_{21}{}^2 k_{ex}}{\left\{ \begin{array}{l} \omega_{e1}{}^2\omega_{e2}{}^2/\omega_e{}^2 + k_{ex}{}^2 - \\ \quad \sin^2\theta\, p_1 p_2 \Delta\omega_{21}{}^2 \left(1 + \dfrac{2k_{ex}{}^2(p_1\omega_{e1}{}^2 + p_2\omega_{e2}{}^2)}{\omega_{e1}{}^2\omega_{e2}{}^2 + \omega_e{}^2 k_{ex}{}^2} \right) \end{array} \right\}} \tag{34}$$

This expression has a simpler form than eq 31 and in most cases is equally or slightly more accurate, as shown in Figure 4. In two special cases, that of equal populations, $p_1 = p_2$, or that of placement of the rf carrier at the average resonance frequency of the two sites, $\omega_{rf} = (\Omega_1 + \Omega_2)/2$, the following result is obtained[26]

$$R_{1\rho} = \bar{R}_1 \cos^2\theta + \bar{R}_2 \sin^2\theta + k_{ex}/2 - \frac{k_{ex}}{2}\left[1 - \frac{4\sin^2\theta\, p_1 p_2 \Delta\omega_{21}{}^2}{\left\{ \begin{array}{l} \omega_{e1}{}^2\omega_{e2}{}^2/\omega_e{}^2 + k_{ex}{}^2 - \\ \quad \sin^2\theta\, p_1 p_2 \Delta\omega_{21}{}^2 \dfrac{k_{ex}{}^2(\omega_{e1}{}^2 + \omega_{e2}{}^2)}{\omega_{e1}{}^2\omega_{e2}{}^2 + \omega_e{}^2 k_{ex}{}^2} \end{array} \right\}} \right]^{1/2} \tag{35}$$

This expression has an improved performance over those of eqs 31 and 34, as illustrated in Figure 5.

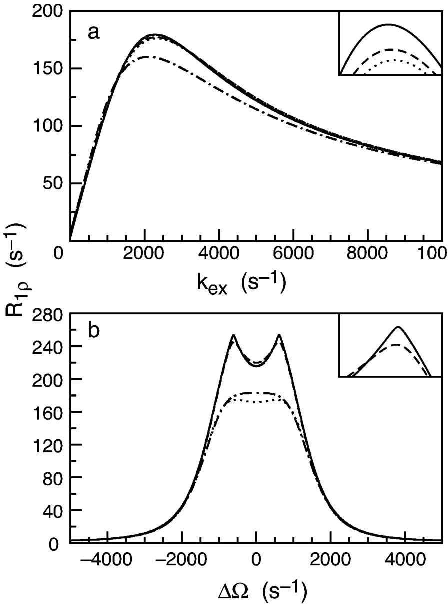

Figure 5. Exchange rate dependence of the $R_{1\rho}$ relaxation rate constant. Shown are (—) the exact numerical eigenvalue, (— - —) the general solution for $p_1 > p_2$ given by eq 31, (•••) the solution given by the linearized Laguerre approximant, eq 34, and (- - -) the solution given by eq 35. Calculations used $\bar{R}_1 = 1.5$ s^{-1}, $\bar{R}_2 = 11$ s^{-1}, $\Delta\omega_{21} = 2400$ s^{-1}, and $\omega_1 = 500$ s^{-1}. In (a) ω_{rf} is set to the average resonance frequency, and $p_1 = 0.7$; the inset shows the region of k_{ex} (1900, 2700), $R_{1\rho}$ (175, 181). In (b) site populations are equal, $p_1 = p_2$, and $k_{ex} = 250$ s^{-1}; the inset shows the region of ΔΩ (300, 850), $R_{1\rho}$ (230, 260). In (b) the abscissa shows $\Delta\Omega = \Omega - \omega_{rf}$.

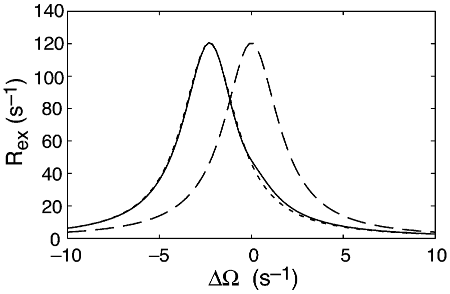

Figure 6. Offset dependence of R_{ex} for two-site exchange. Shown are values of R_{ex} determined using eq 21 from $R_{1\rho}$ calculated from (—) the exact numerical eigenvalue, (- - -) the asymmetric population solution for $p_1 \gg p_2$ given by eq 33, and (— — —) the fast exchange limit solution given by eq 30. Calculations used $\bar{R}_1 = 1.5$ s^{-1}, $\bar{R}_2 = 11$ s^{-1}, $\Delta\omega_{21} = 2400$ s^{-1}, $p_1 = 0.95$, and $\omega_1 = 1000$ s^{-1}, and $\Omega = 1500$ s^{-1}.

The two-site fast exchange solution, eq 30, and the asymmetric populations solution, eq 33, illustrate fundamental differences between fast-limit and intermediate-to-slow exchange regimes for $R_{1\rho}$ relaxation. When exchange is not fast, the exchange broadening is maximal when the carrier is on resonance with the minor state, as predicted by eq 33, rather than the average resonance position, as predicted by eq 30. This offset dependence is most easily observed by plotting R_{ex} versus offset, as shown in Figure 6. Furthermore, if exchange is fast, then only the product $\phi_{ex} = p_1 p_2 \Delta\omega_{21}{}^2$ and $k_{ex} = k_{12} + k_{21}$ can be determined. An independent measurement of the site populations or equilibrium constant is needed to fully characterize the system. Even so, only the magnitude of $\Delta\omega_{21}$ can be determined; the sign is ambiguous. In contrast, if exchange is intermediate-to-slow, then both the site populations and the absolute sign of $\Delta\omega_{21}$ can be determined from the offset dependence of R_{ex}.

The general N-site solution, valid when $p_1 \gg p_i$ for $i = 2$, ..., N, is given by[11]

$$R_{1\rho} = \bar{R}_1 \cos^2\theta + \bar{R}_2 \sin^2\theta + \sum_{i=2}^{N} k_{1i} \mathbf{z}_i{}^{\mathrm{T}} \mathbf{v} \tag{36}$$

in which $\mathbf{z}_i$ is obtained from solving the linear system equations (which always can be done analytically and automatically)

$$\begin{bmatrix} \mathbf{L}'_2 + s_2 \mathbf{1}_s & -k_{23}\mathbf{1}_s & \cdots & -k_{2N}\mathbf{1}_s \\ -k_{32}\mathbf{1}_s & \mathbf{L}'_3 + s_3\mathbf{1}_s & \cdots & -k_{3N}\mathbf{1}_s \\ \vdots & \vdots & \ddots & \vdots \\ -k_{N2}\mathbf{1}_s & -k_{N3}\mathbf{1}_s & \cdots & \mathbf{L}'_N + s_N\mathbf{1}_s \end{bmatrix} \begin{bmatrix} \mathbf{z}_2 \\ \mathbf{z}_3 \\ \vdots \\ \mathbf{z}_N \end{bmatrix} = \begin{bmatrix} \mathbf{L}'_2\mathbf{v} \\ \mathbf{L}'_3\mathbf{v} \\ \vdots \\ \mathbf{L}'_N\mathbf{v} \end{bmatrix} \tag{37}$$

and using the definitions

$$\mathbf{L}'_i = \begin{bmatrix} 0 & -\Omega_i & 0 \\ \Omega_i & 0 & -\omega_1 \\ 0 & \omega_1 & 0 \end{bmatrix} \tag{38}$$

$$\mathbf{v} = \frac{1}{\omega_{e1}} \begin{bmatrix} \omega_1 \\ 0 \\ \Omega_1 \end{bmatrix} \tag{39}$$

For the starlike topology, the general solution reduces to[11]

$$R_{1\rho} = \bar{R}_1 \cos^2\theta + \bar{R}_2 \sin^2\theta + \sin^2\theta \sum_{i=2}^{N} \frac{k_{1i}\Delta\omega_{i1}{}^2}{\Omega_i{}^2 + \omega_1{}^2 + k_{i1}{}^2} \tag{40}$$

The linear three-site model corresponds to $N = 3$ in eq 40 and should be compared to eq 29. When $N = 2$ and $p_1 \rightarrow 1$, eqs 33 and 40 are identical. If exchange between sites 2, ..., N is much slower than exchange between these sites and site 1, i.e., $k_{i1} \gg k_{ij}$ for i, $j = 2$, ..., N, then[11]

$$R_{1\rho} = \bar{R}_1 \cos^2\theta + \bar{R}_2 \sin^2\theta + \sin^2\theta \sum_{i=2}^{N} \frac{k_{1i}}{\Omega_i{}^2 + \omega_1{}^2 + s_i{}^2} \Bigg\{ \Delta\omega_{i1}{}^2 + \frac{1}{s_i} \sum_{\substack{j=3 \\ i\neq j}}^{N} \frac{k_{ij}}{\Omega_j{}^2 + \omega_1{}^2 + s_j{}^2} (\Delta\omega_{ji}(\omega_1{}^2 + \Omega_1\Omega_i) + s_i{}^2\Delta\omega_{j1} + s_i s_j \Delta\omega_{i1}) \Bigg\} \tag{41}$$

This expression reduces to eq 40 if $k_{ij} = 0$ for i, $j = 2$, ..., N. If exchange between sites 2, ..., N is much faster than exchange between these sites and site 1, i.e., $k_{i1} \ll k_{ij}$ for i, $j = 2$, ..., N, then eqs 15−19 yield[11]

$$R_{1\rho} = \bar{R}_1 \cos^2\theta + \bar{R}_2 \sin^2\theta + \sin^2\theta \frac{k'_{12}}{\Omega'^2_2 + \omega_1{}^2 + k'^2_{21}} \tag{42}$$

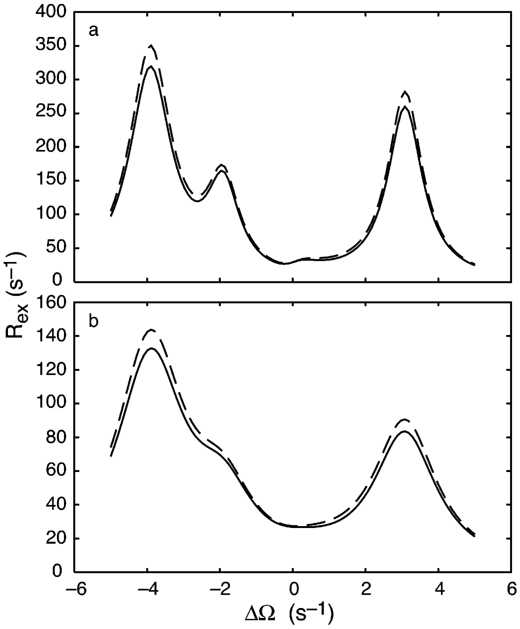

Figure 7. Offset dependence of R_{ex} for a four-site system with starlike topology. Shown are (—) the exact numerical eigenvalue and (- - -) the approximate solution obtained from eq 40. Curves were calculated using (a) $\omega_1 = 500$ s^{-1} and (b) $\omega_1 = 1000$ s^{-1}. Other parameters used in the calculations were as follows: $p_1 = 0.90$, $p_2 = 0.05$, $p_3 = 0.03$, $p_4 = 0.02$, $\Delta\omega_{21} = 2000$ s^{-1}, $\Delta\omega_{31} = -3000$ s^{-1}, $\Delta\omega_{41} = 4000$ s^{-1}, $k_{12} + k_{21} = 200$ s^{-1}, $k_{13} + k_{31} = 200$ s^{-1}, $k_{14} + k_{41} = 4200$ s^{-1}, $\bar{R}_1 = 1.5$ s^{-1}, and $\bar{R}_2 = 11$ s^{-1}. The abscissa shows $\Delta\Omega = \Omega - \omega_{rf}$.

in which

$$\Omega_2' = (1 - p_1)^{-1}\sum_{i=2}^{N} p_i\Omega_i \tag{43}$$

In eqs 40−42, the substitution has been made that $\omega_1/\omega_{e1} \approx \omega_1/\omega_e = \sin\theta$.

The accuracy of eq 40 is illustrated in Figure 7 for a four-site exchange process with a starlike topology. The important qualitative result is that the graph of R_{ex} versus resonance offset consists of $N - 1$ Lorentzian-shaped peaks with local maxima occurring when $\Omega_i = 0$ for $i = 2, ..., N$. The ith Lorentzian has a full-width-at-half-height equal to $2(k_{i1}{}^2 + \omega_1{}^2)^{1/2}$. Consequently, the number of components in the R_{ex} profile is most easily discerned when ω_1 is weak, preferably $\omega_1 \leq k_{i1}$, as indicated by comparison of parts a and b of Figure 7.

Some aspects of three-site exchange are exhibited by Figures 8 and 9. In Figure 8, R_{ex} for the linear three-site model, eq 12, determined using eq 40, is compared with a more general model in which slow exchange occurs between sites 2 and 3, calculated using eq 41. The main qualitative effect of exchange between sites 2 and 3 is an overall increase in the value of R_{ex}. In Figure 9, the effect of the rate of exchange between sites 2 and 3 is illustrated for the linear three-site model, eq 13. When $k_{23} + k_{32} \rightarrow 0$, exchange is accurately described as a two-state process involving only sites 1 and 2. When $k_{23} + k_{32}$ is appreciable, then the three-site process is manifest by the appearance of two Lorentizian peaks in the plot of R_{ex} versus offset. When $k_{23} + k_{32} \rightarrow \infty$, exchange is described as a two-state process between site 1 and an effective average of the properties of sites 2 and 3, as given by eqs 15−19. Finally, as shown by comparing parts a and b of Figure 9, the shape of the R_{ex} versus offset profiles depends strongly on the rate of exchange between sites 1 and 2.

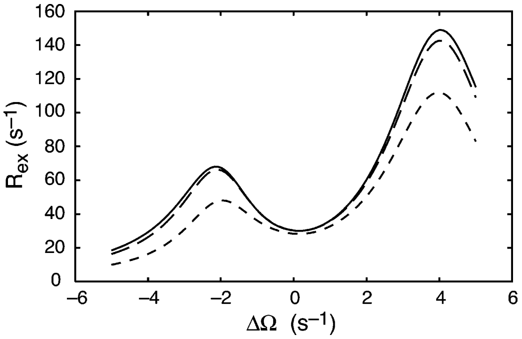

Figure 8. Offset dependence of R_{ex} for a general three-site system. Shown are (—) the exact numerical solution, (— — —) the approximate solution obtained from eq 41, and (- - -) the approximate solution obtained from eq 40 for the starlike topology. The solid and long-dashed curves were calculated using $k_{23} + k_{32} = 700$ s^{-1}; the short-dashed curve was calculated using $k_{23} + k_{32} = 0$ s^{-1}. Other parameters used in the calculations were as follows: $\omega_1 = 1000$ s^{-1}, $p_1 = 0.95$, $p_2 = 0.03$, $p_3 = 0.02$, $\Delta\omega_{21} = 2000$ s^{-1}, $\Delta\omega_{31} = -4000$ s^{-1}, $k_{12} + k_{21} = 500$ s^{-1}, $k_{13} + k_{31} = 1000$ s^{-1}, $\bar{R}_1 = 1.5$ s^{-1}, and $\bar{R}_2 = 11$ s^{-1}. The abscissa shows $\Delta\Omega = \Omega - \omega_{rf}$.

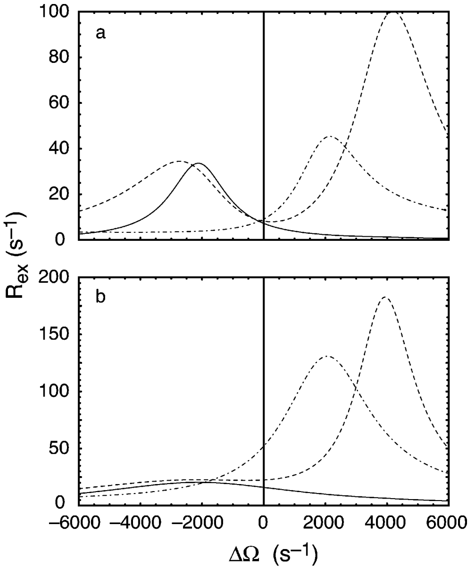

Figure 9. Time-scale dependence of R_{ex} for a linear three-site system. Curves were calculated using eq 36 for (—) $k_{23} + k_{32} = 1$ s^{-1}, (- - -) $k_{23} + k_{32} = 1000$ s^{-1}, and (− - −) $k_{23} + k_{32} = 100\,000$ s^{-1}. In (a) $k_{12} + k_{21} = 500$ s^{-1}, and in (b) $k_{12} + k_{21} = 2000$ s^{-1}. Other parameters used in the calculations were as follows: $\omega_1 = 1000$ s^{-1}, $p_1 = 0.94$, $p_2 = 0.02$, $p_3 = 0.04$, $\Delta\omega_{21} = 2000$ s^{-1}, $\Delta\omega_{31} = -4000$ s^{-1}, $k_{13} + k_{31} = 0$ s^{-1}, $\bar{R}_1 = 1.5$ s^{-1}, and $\bar{R}_2 = 11$ s^{-1}. The abscissa shows $\Delta\Omega = \Omega - \omega_{rf}$.

Expressions for the $R_{2\rho}$ relaxation rate constant have been derived only for fast exchange limit kinetic processes.[12,27] In the fast exchange regime, a general solution for N-site exchange is[12]

$$R_{2\rho} = \bar{R}_1 \sin^2\theta + \bar{R}_2 \cos^2\theta + \sin^2\theta \sum_{i=2}^{N} \frac{|\langle u_1|\Omega|u_i\rangle|^2}{\lambda_i}\left(1 + \frac{\lambda_i{}^2}{2(\lambda_i{}^2 + \omega_e{}^2)}\right) \tag{44}$$

The exchange contribution to $R_{2\rho}$ is the sum of the free-precession broadening plus 0.5 times the exchange contribu-

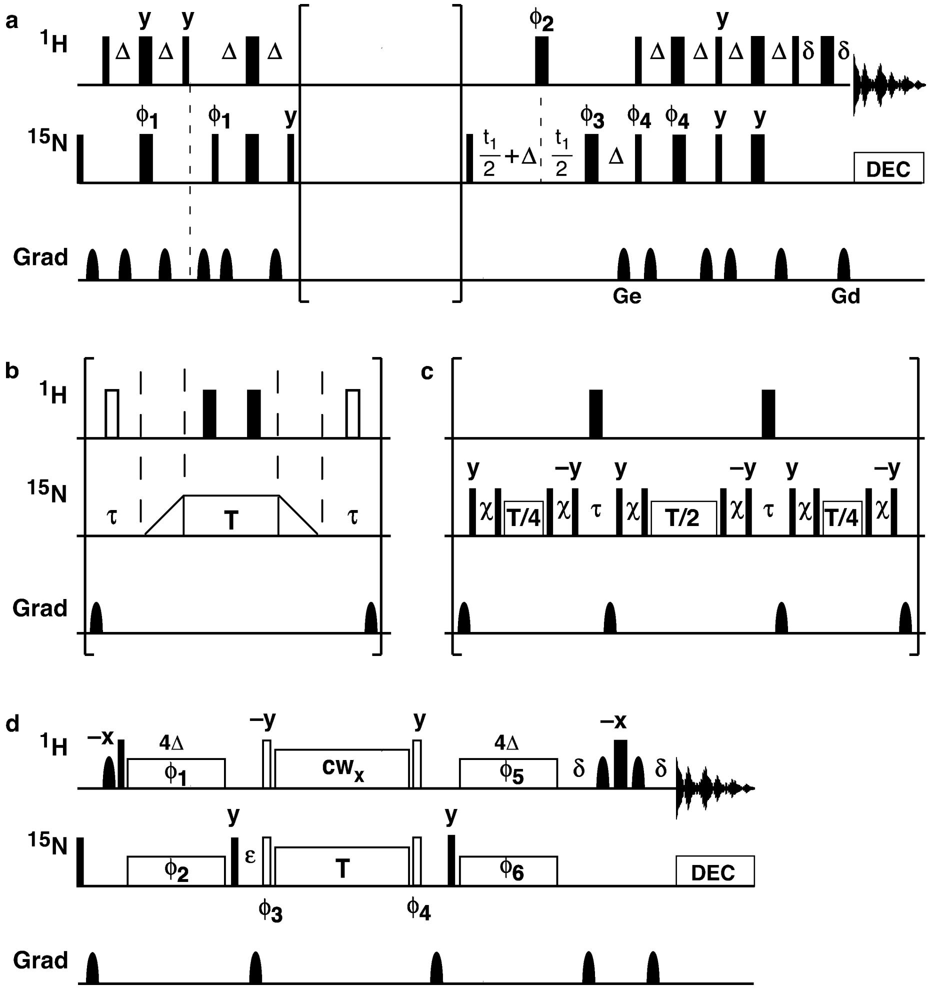

Figure 10. Pulse sequences for ^{15}N $R_{1\rho}$ relaxation measurements. Narrow and wide bars indicate 90° and 180° pulses, respectively. All pulses are applied with phase x unless otherwise indicated. Delays are $\Delta = {}^{1}/_{4}J_{\mathrm{NH}}$, and δ is long enough to encompass the enclosed gradients and gradient recovery delays. ^{15}N decoupling during acquisition is performed using a GARP[72] or other decoupling sequence. (a) The basic pulse sequence for on- and off-resonance $R_{1\rho}$ measurements. The phase cycle is as follows: $\phi_1 = x, -x$; $\phi_2 = 4(x), 4(-x)$; $\phi_3 = 2(x), 2(y), 2(-x), 2(-y)$; $\phi_4 = x$; $\phi_{\mathrm{rec}} = x, -x, -x, x$. Gd and Ge are used for gradient coherence selection. Gradient PEP coherence selection is obtained by inverting the sign of gradient Gd and phase ϕ_4.[44,45] In (b) and (c) open rectangles indicate ^{15}N spin-lock periods, always applied with phase x. The total length of the spin-lock period is equal to T. In a conventional $R_{1\rho}$ experiment the delays τ are set just long enough to encompass the gradient and gradient recovery delays, and the 180° ^{1}H pulses represented as open bars are not included. In a $R_{1\rho} - R_1$ experiment, the value $\tau = \tau_{\max} - T/2$, in which $\tau_{\max}$ is equal to the sum of the length of the gradient, the gradient recovery delay, and half of the maximum value of the relaxation period, $T_{\max}$. (b) Off-resonance $R_{1\rho}$ experiment obtained by inserting the bracketed segment into (a). The triangles represent the adiabatic sweeps that rotate the magnetization from the z-azis to the direction of the effective field, and back to the z-axis.[30] (c) On-resonance $R_{1\rho}$ experiment obtained by inserting the bracketed segment into (a). Magnetization is aligned along the effective field by the element $90°-\chi-90°$, where $\chi = 1/\omega_1$, and ω_1 is the spin-lock field strength. (d) Selective one-dimensional on- and off-resonance $R_{1\rho}$ experiment. Shaped ^{1}H pulses are selective 90° pulses used for Watergate water suppression.[1] Open ^{15}N bars indicate pulses with a tip angle equal to $\arctan(\omega_1/\Omega)$, where Ω is the ^{15}N resonance offset from the spin-lock carrier. Open ^{1}H bars indicate pulses with tip angle equal to $\arctan(\omega_{1I}/\Omega_{\mathrm{W}})$, where ω_{1I} is the strength of the ^{1}H cw field applied during the spin lock and Ω_{W} is the resonance offset from the frequency of water. Open rectangles on ^{1}H indicate cw fields. The strength of the ^{1}H cw field applied during the spin-lock period is equal to $\omega_{1S}/2\pi = 3900$ Hz. The strength of the cw fields applied on ^{1}H and ^{15}N synchronously during the polarization transfer period is $\approx$90 Hz. After the first water selective pulse, the ^{1}H carrier is shifted to the amide resonance of interest and is placed back on the water signal prior to the Watergate element. The ^{15}N carrier is placed on the amide resonance of interest during the polarization transfer and shifted to the desired off-resonance position Ω during the spin-lock period T. The phase cycle is as follows: $\phi_1 = 8(y), 8(-y)$; $\phi_2 = -x, x$; $\phi_5 = 4(x), 4(-x)$; $\phi_6 = 2(x), 2(-x)$; $\phi_{\mathrm{rec}} = x, -x, -x, x, -x, x, x, -x, x, -x, -x, x$; for $\Omega_S < 0$, $\phi_3 = -y$ and $\phi_4 = y$; for $\Omega_S > 0$, $\phi_3 = y$; $\phi_4 = -y$.

tion to $R_{1\rho}$. This result is anticipated on general physical grounds and indicates that $R_{2\rho}$ does not provide unique additional information about a fast exchange process.

3. Experimental Methods

Pulse sequences for $R_{1\rho}$ measurements can be categorized variously as “off-resonance” or “on-resonance” (often called “near-resonance”), depending on the size of Ω, or as “strong field” and “weak-field”, depending on the magnitude of ω_1. The pulse sequences discussed below have been designed for application to ^{15}N, ^{1}H$^{\mathrm{N}}$, ^{13}CO, and ^{13}C$^{\alpha}$ nuclear spins in proteins; however, the modifications necessary for application to nucleic acids, particularly the isolated ^{13}C spins of the C-2 and C-8 positions of adenine and the C-8 positions of guanine nucleotides, are straightforward.[28,29]

3.1. Pulse Sequences for ^{15}N $R_{1\rho}$ Measurements

The pulse sequences for ^{15}N $R_{1\rho}$ measurements in backbone N−H spin systems in proteins are shown in Figure 10.

A two-dimensional pulse sequence for off-resonance, strong-field measurements is shown in Figure 10a and b.[30−32] A two-dimensional pulse sequence for on-resonance, weak-field $R_{1\rho}$ measurements is shown in Figure 10a and c.[8] A selective one-dimensional pulse sequence is shown in Figure 10d; this sequence can be used for both strong and weak ω_1 fields and for both on- or off-resonance experiments.[7]

The first two pulse sequences use conventional refocused INEPT techniques for polarization transfer between ^{1}H and ^{15}N spins. These polarization transfers are broad-band and allow spectra to be recorded as two-dimensional data sets for optimal resolution of resonance signals. The pulse sequences as depicted use an heteronuclear single-quantum coherence (HSQC) experiment for recording two-dimensional spectra. The HSQC element can be replaced by a transverse relaxation optimized spectroscopy (TROSY) experiment for improved sensitivity and resolution for large proteins at high static magnetic field strengths.[33,34] The third pulse sequence uses selective cross-polarization to transfer magnetization between a single ^{1}H spin and its attached ^{15}N spin.[7,35,36] Selective excitation of a single ^{15}N spin allows one-dimensional spectroscopy to be employed. If necessary, as discussed elsewhere,[7] a ^{15}N jump-return element can be incorporated into the pulse sequence to further increase selectivity.

When exchange is not fast on the chemical shift time scale, selective excitation can affect the initial conditions at the start of the relaxation period. An assumption inherent in the derivation of the above expressions for $R_{1\rho}$ is that the initial state of the spin-locked magnetization is proportional to $\mathbf{P}$, the equilibrium site populations. To ensure that this condition is met even for selective excitation of a single site, as in Figure 10d, magnetization is returned to the z-axis in the laboratory reference frame for a time period, ϵ, long enough to allow exchange of longitudinal magnetization to equilibrate the site magnetizations. For two-site exchange, $\epsilon > 1/k_{\mathrm{ex}} - 3/k_{\mathrm{ex}}$ is sufficient.

For all three pulse sequences, S ($= {}^{15}$N) magnetization must be aligned parallel to the effective field in the doubly rotating tilted frame (Figure 1). Alignment is achieved by different approaches in the three pulse sequences. In Figure 10d, S_z magnetization is transformed to S'_z magnetization by applying a hard pulse with y-phase and rotation angle given by $\tan\theta = \omega_1/\Omega$, where Ω is the offset of the selectively excited resonance. This approach is accurate only for a single selective value of Ω, and the error in the alignment is given approximately by $\sin^2\theta\,\Delta\Omega/\omega_1$, in which $\Delta\Omega$ is the offset from Ω. In Figure 10c, the desired transformation is effected by using the pulse sequence element $90^\circ_\phi - \chi - 90^\circ_{\phi+\pi}$, in which $\chi = 1/\omega_1$.[37] Good alignment is obtained for $-0.4\omega_1 < \Omega < 0.4\omega_1$, corresponding to $68^\circ < \theta < 112^\circ$.[8] In Figure 10b, magnetization is aligned using an adiabatic sweep.[30,32] Provided that ω_1 is sufficiently strong, good alignment is obtained over a bandwidth that encompasses the entire ^{15}N spectral width. Using the pulse sequence of Figure 10a and b, $R_{1\rho}$ is measured simultaneously for all ^{15}N spins from a single time series of two-dimensional spectra. Using the pulse sequence of Figure 10a and c, $R_{1\rho}$ is measured simultaneously for a subset of ^{15}N spins from each time series of two-dimensional spectra. The relaxation rate constants for the full set of ^{15}N spins are obtained by recording multiple time series with different rf carrier frequencies. Using the pulse sequence of Figure 10d, $R_{1\rho}$ is measured independently for each spin of interest (which may be a much smaller number than the total number of ^{15}N spins in a molecule).

The pulse sequences shown in Figure 10 apply rf fields at the ^{1}H Larmor frequency, as either rf pulses or CW fields, to suppress cross-correlation between ^{1}H−^{15}N dipole−dipole and ^{15}N chemical shift anisotropy relaxation mechanisms. The application of ^{1}H rf fields while the ^{15}N magnetization is spin-locked can result in reintroduction of the heteronuclear scalar coupling Hamiltonian.[8,13]

If continuous wave rf fields are applied to both I (^{1}H) and S (^{15}N) spins during the relaxation delay T, then the Hamiltonian in the rotating frames of the I and S spins is

$$\mathscr{H} = \Omega_I I_z + \omega_{1I} I_x + \Omega_S S_z + \omega_{1S} S_x + 2\pi J_{IS} I_z S_z \quad (45)$$

in which Ω_I (Ω_S) is the resonance offset of the I (S) spins, ω_{1I} (ω_{1S}) is the applied rf field for the I (S) spins, and J_{IS} is the scalar coupling constant. This Hamiltonian can be transformed to a doubly rotating tilted reference frame for both I and S spins. These frames have I'_z and S'_z axes tilted by θ_I and θ_S and are rotating with frequencies $\omega_{\mathrm{e}I}$ and $\omega_{\mathrm{e}S}$, respectively, relative to the singly rotating reference frames. In the present discussion, ω_{1S} and $\omega_{\mathrm{e}S}$ are identical to ω_1 and ω_{e} in the expressions for $R_{1\rho}$ given above. The first-order average Hamiltonian in the tilted, doubly rotating reference frame is[8]

$$\bar{\mathscr{H}} = 2\pi J_{IS}[I'_z S'_z \cos\theta_I \cos\theta_S - I'_z S'_x \cos\theta_I \sin\theta_S\, \mathrm{sinc}(\omega_{\mathrm{e}S}T/2)] \quad (46)$$

under the assumptions, applicable to the present experimental design, that $\omega_{\mathrm{e}I} \gg \omega_{\mathrm{e}S}$ and $\omega_{\mathrm{e}I}T/2\pi \gg 1$. The spin-locked S'_z magnetization aligned with the effective field commutes with the first term in eq 46. The second term is negligible if either $T = 2n\pi/\omega_{\mathrm{e}S}$, with n a nonzero integer, or $\omega_{\mathrm{e}S}T/2\pi \gg 1$. These conditions govern appropriate choices of T in the experiment shown in Figure 10d. This experiment is compatible with a range of ^{15}N rf fields from $\omega_1/2\pi = 25$ Hz to 1000 Hz. The main drawback to the experiment is that relatively strong ^{1}H rf fields ($\omega_{1I} \approx 4$ kHz) must be applied to satisfy the conditions leading to the above average Hamiltonian.

The situation is more complicated if periodic ^{1}H hard 180° pulses are applied while the ^{15}N magnetization is spin-locked, as shown in Figure 10b. The effect of the pulses is to invert the sign of J_{IS} at points $T/4$ and $3T/4$. The Hamiltonian in the rotating frame of the S spin is

$$\mathscr{H} = \Omega_S S_z + \omega_{1S} S_x + 2\pi a(t) J_{IS} I_z S_z \quad (47)$$

in which $a(t)$ is the effective sign of J_{IS} due to the inversion by the ^{1}H 180° pulses. The Hamiltonian is transformed to the doubly rotating tilted frame of the S spins. In this case, the average Hamiltonian is[8]

$$\bar{\mathscr{H}} = J_{IS} I'_z S'_x \sin\theta_S\, \mathrm{sinc}(\omega_{\mathrm{e}S}T/2)\left[-\pi - \psi\left(\frac{1 - \omega_{\mathrm{e}S}T/2\pi}{4}\right) + \psi\left(\frac{3 - \omega_{\mathrm{e}S}T/2\pi}{4}\right)\right] \quad (48)$$

in which $\psi(x)$ is the digamma function.[38] Provided that $2\pi J_{IS}/\omega_1 \ll 1$, typically <0.2, then numerical calculations show that the effect of the residual scalar coupling Hamiltonian is negligible.

The pulse sequence shown in Figure 10c avoids reintroducing the scalar coupling interaction by returning the magnetization from the tilted to laboratory *z*-axes prior to applying ^{1}H 180° pulses. This experiment has been shown empirically to be effective for $2\pi J_{IS}/\omega_1 < 0.6$.[8]

The pulse sequences shown in Figure 10b and c can be performed either as conventional $R_{1\rho}$ experiments or as $R_{1\rho} - R_1$ experiments.[31] In the former, the 180° pulses shown as open bars during the delays τ in Figure 10b are not included. In both parts b and c of Figure 10, τ is set just long enough to encompass the gradient, gradient recovery delays, and any pulses. In the latter case, the value of $\tau = \tau_{max} - T/2$, in which τ_{max} is equal to the sum of the length of the gradient, the gradient recovery delay, and half of the maximum value of the relaxation period, $T_{max}/2$. The average effective relaxation rate constant in this experiment is given by[31]

$$\begin{aligned} R_{eff} &= R_{1\rho} - \bar{R}_1 \\ &= \bar{R}_1 \cos^2\theta + \bar{R}_2 \sin^2\theta + R_{ex} \sin^2\theta - \bar{R}_1 \\ &= \bar{R}_1(\cos^2\theta - 1) + \bar{R}_2 \sin^2\theta + R_{ex}\sin^2\theta \\ &= (\bar{R}_2 - \bar{R}_1 + R_{ex}) \sin^2\theta \end{aligned} \tag{49}$$

which gives

$$R_{ex} = R_{eff}/\sin^2\theta - \bar{R}_2 + \bar{R}_1 \tag{50}$$

as an alternative formulation of R_{ex} compared to eq 21.

Examples of ^{15}N $R_{1\rho}$ relaxation dispersion data are shown in Figure 11 for backbone amide spins of Cys14 and Lys15 in basic pancreatic trypsin inhibitor. Previous investigations by CPMG relaxation dispersion have shown that chemical exchange line broadening arises from transitions of the side chain of Cys14 between χ_1 rotamers.[39] Figure 11a illustrates the offset dependence of $R_{1\rho}$ predicted by eq 33: when exchange is not fast, then different values of R_{ex} are obtained for ω_{rf} positioned symmetrically on either side of the observed resonance. The broad range of effective fields that can be accessed using combinations of strong and weak rf fields is illustrated in Figure 11b.

3.2. Pulse Sequences for ^{1}H and ^{13}C $R_{1\rho}$ Measurements

Recently, pulse sequences for $R_{1\rho}$ relaxation measurements in ^{1}H^N, ^{13}CO, and ^{13}C$^\alpha$ spin systems have been reported.[14−17,40] Pulse sequences for ^{1}H^N $R_{1\rho}$ measurements in backbone N−H spin systems in proteins are shown in Figure 12. A pulse sequence for on-resonance measurements is shown in Figure 12b.[14] Two different pulse sequences for off-resonance measurements are shown in Figure 12c[40] and d.[17] The sequence shown in Figure 12d uses the $R_{1\rho} - R_1$ approach.[31] Pulse sequences for ^{13}CO and ^{13}C$^\alpha$ $R_{1\rho}$ relaxation measurements are shown in parts a[15] and b,[16] respectively, of Figure 13.

The main differences between these experiments and the ^{15}N $R_{1\rho}$ techniques are that homonuclear scalar coupling evolution and dipole−dipole cross-relaxation during the spin-locking periods must be considered. For ^{1}H^N $R_{1\rho}$ measurements, the ^{1}H^N−^{1}H$^\alpha$ scalar coupling interaction can be eliminated by preparing proteins that are deuterated at aliphatic carbon positions;[14,41] alternatively, band-selective 180° pulses also can be used for decoupling.[40] For ^{13}C $R_{1\rho}$ measurements, ^{13}C−^{13}C scalar coupling interactions can be reduced or eliminated by preparing fractionally or alternately ^{13}C enriched proteins, as has been done for conventional laboratory frame relaxation studies.[42,43] To date, however, reported applications have used fully ^{13}C enriched proteins. In these circumstances, Hartmann−Hahn transfer from ^{13}C S_1 to ^{13}C S_2 is described by[1]

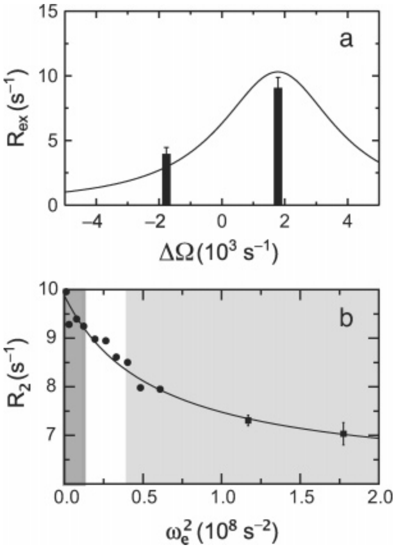

Figure 11. BPTI relaxation dispersion. (a) The solid bars depict the conformational exchange contribution to transverse relaxation, R_{ex}, of Lys 15 for values of $\Delta\Omega = \Omega - \omega_{rf}$ approximately given by $\pm\Delta\omega_{12}$. R_{ex} data are obtained from $R_{1\rho}$ data using eq 21. $\bar{R}_1$ was measured independently by conventional techniques.[73] $\bar{R}_2$ was estimated from the relaxation interference rate constant as described elsewhere.[74,75] The solid line shows the fit to eq 33 using $\bar{R}_1 = 1.5$ s^{-1}, $\bar{R}_2 = 6.8$ s^{-1}, $p_1 = 0.984$, $p_2 = 0.016$, $k_{ex} = 1100$ s^{-1}, $\Delta\omega_{21} = 1780$ s^{-1}, and $\omega_1/2\pi = 314$ Hz determined from CPMG relaxation dispersion.[39] (b) R_2 values for Cys14 of BPTI measured at a magnetic field of 14.1 T are plotted versus the effective field, ω_e.[28] R_2 data are obtained from $R_{1\rho}$ data using eq 20. Points represented as circles have been calculated from on-resonance $R_{1\rho}$ rates measured using the pulse sequence presented in Figure 10c; points represented as squares have been calculated from off-resonance $R_{1\rho}$ rates measured using the pulse sequence shown in Figure 10b. The solid line shows the fit for the fast exchange limit, eq 30, with $k_{ex} = 7600 \pm 200$ s^{-1} and $p_1p_2\Delta\omega_{21}{}^2 = 28\,800 \pm 800$ s^{-2}. The dark gray and light gray areas of the plot represent the range of effective fields respectively accessible to CPMG ($\tau_{cp} \geq 1$ ms) and strong-field $R_{1\rho}$ ($\omega_1/2\pi \geq 1000$ Hz) experiments, respectively.

$$S'_{z1} \xrightarrow{T} S'_{z1}\{1 - \sin^2\phi \sin^2(qT)\} + S'_{z2} \sin^2\phi \sin^2(qT) \tag{51}$$

in which

$$\begin{aligned} q &= [(\omega_{e1} - \omega_{e2})^2 + (\pi J_{CC} \sin\theta_1 \sin\theta_2)^2]^{1/2} \\ \tan\phi &= \frac{1}{2}\left(\frac{2\pi J_{CC} \sin\theta_1 \sin\theta_2}{\omega_{e1} - \omega_{e2}}\right) \end{aligned} \tag{52}$$

If the resonance frequencies are sufficiently different, such as for ^{13}CO and ^{13}C$^\alpha$, or for ^{13}C$^\alpha$ and ^{13}C$^\beta$ in most amino acids, values of ω_1 and ω_{rf} can be chosen to keep $\sin^2\phi < 0.01$, in which case the effects of Hartmann−Hahn matching are insignificant. However, for certain pairs of spins with very similar resonance frequencies, such as backbone ^{13}CO and ^{13}C$^\gamma$ in Asp and Asn residues or ^{13}C$^\alpha$ and ^{13}C$^\beta$ in Ser and Thr residues, the effects of Hartman−Hahn matching may be sufficiently large that the relaxation rate constants cannot be reliably measured.[15,16]

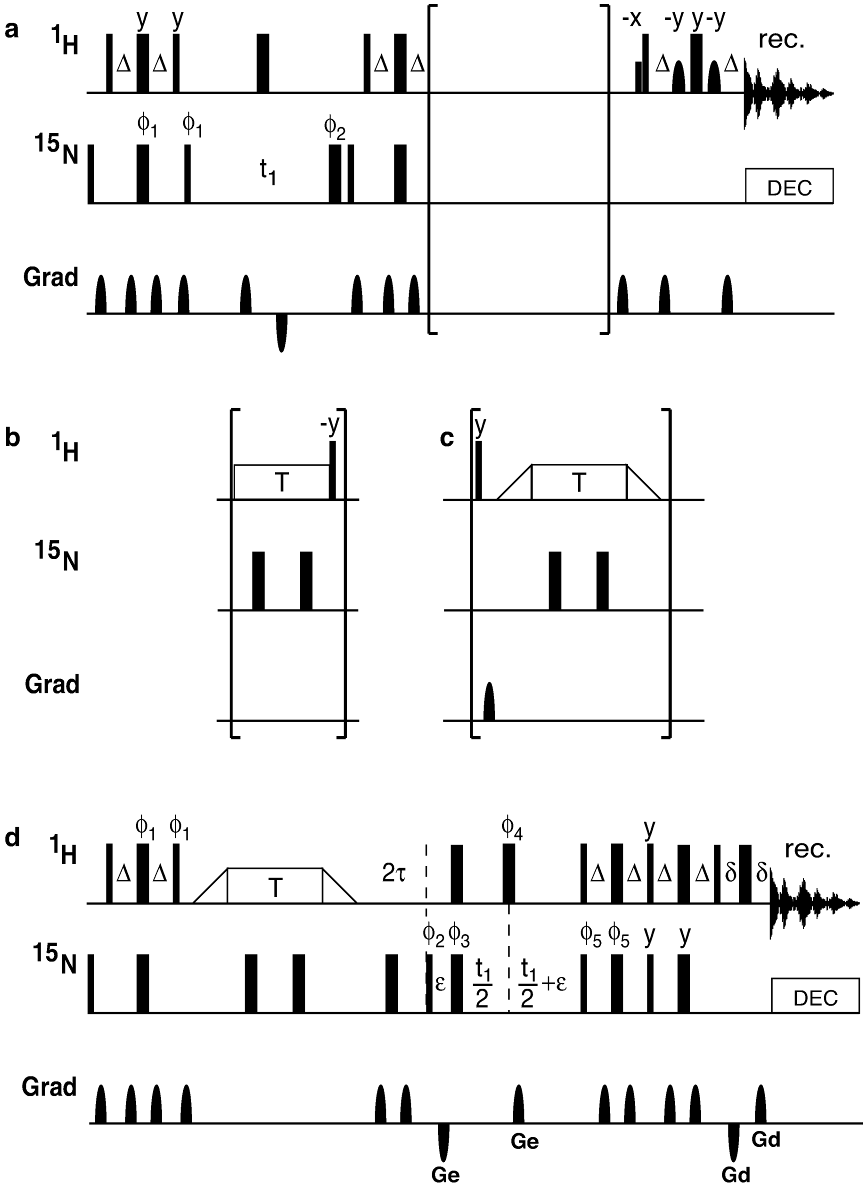

Figure 12. Pulse sequences for ^{1}H $R_{1\rho}$ relaxation measurements. Unless noted, experimental details are the same as those given in the caption of Figure 10. (a) The basic pulse sequence for on- and off-resonance ^{1}H $R_{1\rho}$ measurements. The phase cycle is as follows: $\phi_1 = x, -x$; $\phi_2 = 2(x), 2(y), 2(-x), 2(-y)$; $\phi_{\text{rec}} = x, -x, -x, x$. The ^{1}H carrier is set resonant with the water signal, except during the spin-lock period, when the carrier is moved to 8.3 ppm. Quadrature detection in the t_1 dimension is achieved by States-TPPI phase cycling of ϕ_1 and of the receiver.[76] (b) ^{1}H on-resonance and (c) ^{1}H off-resonance $R_{1\rho}$ relaxation experiments, respectively, for in-phase ^{1}H^N magnetization obtained by inserting the bracketed elements into (a). (d) ^{1}H off-resonance $R_{1\rho} - R_1$ relaxation experiment for two-spin coherence. ϵ is long enough to encompass the gradient Ge and the recovery delays. The phase cycle is as follows: $\phi_1 = y, -y$; $\phi_2 = 2(x), 2(-x)$; $\phi_3 = 4(x), 4(y), 4(-x), 4(-y)$; $\phi_4 = x$; $\phi_5 = x$; $\phi_{\text{rec}} = x, -x, -x, x, -x, x, x, -x$. Quadrature detection in t_1 is implemented by inverting the phase of ϕ_5 together with the sign of Ge.[44,45]

For ^{1}H^N $R_{1\rho}$ experiments, the effects of ^{1}H−^{1}H dipole−dipole cross-relaxation, due to the NOE, also are significant. Even in deuterated proteins, dipole−dipole interactions exist between ^{1}H^N spins and other exchangeable hydrogen atoms, such as other ^{1}H^N spins and hydroxyl ^{1}H spins. Two approaches have been utilized to minimize these effects.

In the first approach, the pulse sequence is designed to ensure that the ^{1}H^N spins relax with selective dipole−dipole relaxation rate constants during the spin-locking period. Two strategies have been employed to achieve this aim. In one strategy, the t_1 period is placed before the spin-locking period, as shown in Figure 12a and b.[14,40] In the other strategy, shown in Figure 12c, relaxation of the two-spin order operator, $2I_zS'_z$ (in this operator, $I = {}^{15}$N and $S = {}^1$H^N), is recorded, rather than that of pure S'_z.[17] The second technique has the advantage that sensitivity-enhanced detection schemes can be used, with a $2^{1/2}$ gain in sensitivity.[44,45]

In the second approach, which can be combined with the first approach, as shown in Figure 12c, S'_z magnetization is spin-locked at an angle $\theta = 35°$. Under this condition and assuming the macromolecular spin-diffusion limit for relaxation, $\tau_c\omega \gg 1$, the NOE and ROE cross-relaxation rate constants mutually cancel.[46] In this case, relaxation dispersion curves are measured by covarying ω_1 and Ω to vary ω_e while keeping θ constant. An experimental difficulty with this technique arises because the $\theta = 35°$ condition cannot be met simultaneously for all spins in the spectrum due to resonance dispersion. This difficulty can be circumvented

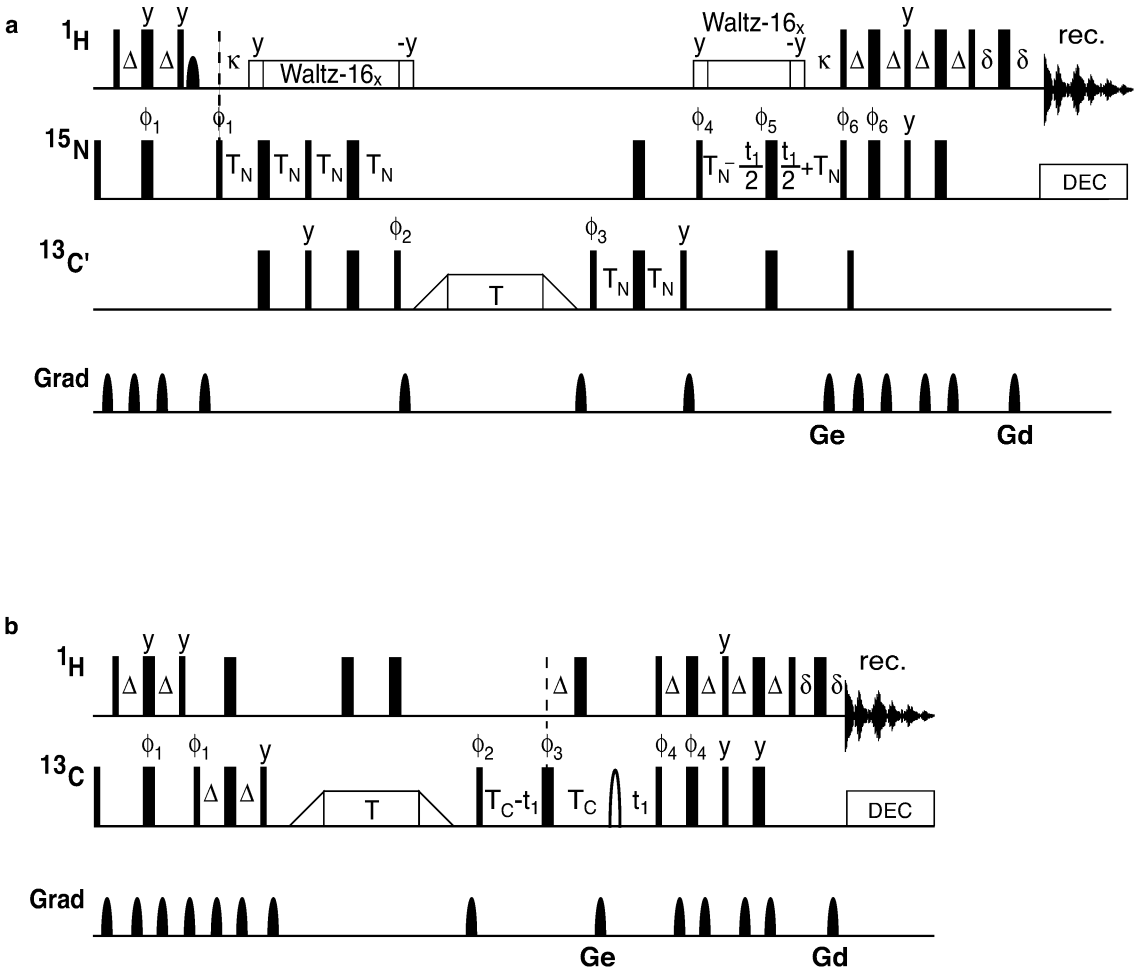

Figure 13. Pulse sequences for ^{13}CO and ^{13}C$^{\alpha}$ $R_{1\rho}$ relaxation measurements. Unless noted, experimental details are the same as those given in the caption of Figure 10. (a) ^{13}CO off-resonance $R_{1\rho}$ relaxation experiment. ^{1}H decoupling is performed with a Waltz-16 sequence.[77] Flanking 90° pulses serve to align the water magnetization along the Waltz-16 rf field before decoupling and to return water magnetization back to the z-axis after decoupling. ^{13}CO pulses are centered in the middle of the carbonyl region and calibrated to have an excitation null in the ^{13}C$^{\alpha}$ region of the spectrum. The delays are $\kappa = 2\Delta$ and $T_N = 1/(4J_{\mathrm{NCO}})$. The phase cycle is as follows: $\phi_1 = x, -x$; $\phi_2 = 2(x), 2(-x)$; $\phi_3 = 4(x), 4(-x)$; $\phi_4 = 8(x), 8(-x)$; $\phi_5 = 4(x), 4(-x)$; $\phi_6 = x$; $\phi_{\mathrm{rec}} = x, 2(-x), x, -x, 2(x), 2(-x), 2(x), -x, x, 2(-x), x$. (b) ^{13}C$^{\alpha}$ off-resonance $R_{1\rho}$ relaxation experiment. The shaped open pulse during the constant time evolution period is used to selectively invert the ^{13}CO spins. The delay values are $\Delta = 1/(4J_{\mathrm{CH}})$ and $T_{\mathrm{C}} = 1/(4J_{\mathrm{CC}})$. The phase cycle is as follows: $\phi_1 = x, -x$; $\phi_2 = x$; $\phi_3 = 2(x), 2(y), 2(-x), 2(-y)$; $\phi_4 = x$; $\phi_{\mathrm{rec}} = x, -x, -x, x$.

by recording spectra in an interleaved fashion using rf carrier positions positioned symmetrically upfield and downfield of the center of the NMR spectrum.[17,47,48]

3.3. Experimental Considerations for $R_{1\rho}$ Relaxation

Obtaining the most accurate and precise $R_{1\rho}$ measurements necessitates careful optimization of experimental conditions. Temperature control, water suppression, and calibration of ω_1 rf fields are particularly important.

3.3.1. Temperature Control

Proper control of the sample temperature, important in all spin relaxation measurements, is critical in $R_{1\rho}$ experiments because conformational dynamics on microsecond to millisecond time scales typically are extremely temperature dependent and because significant heating effects can arise from application of strong rf fields. The main approach to temperature regulation is to ensure that the same total rf power is deposited into the sample for each free-induction decay (FID) recorded.[49] This is achieved by applying a compensating spin-lock field during the beginning of the interscan recycle delay for a time period T_{comp}. The spin lock is applied within the recycle delay so that the recovery of ^{1}H magnetization between scans is identical for all FIDs. Accordingly, any ^{1}H spin-lock fields must be applied far enough off resonance to avoid perturbing ^{1}H magnetization.[40,49] However, the rf carrier should not be positioned so far off-resonance that the rf is being applied outside the ideal tuning range of the probe. If a constant value of ω_1 is used for the entire dispersion experiment, then $T_{\mathrm{comp}} = T_{\max} - T$. If ω_1 is varied during the course of the dispersion experiment, then T_{comp} is adjusted so that $T_{\mathrm{comp}}\omega_{1\max}{}^2 + T\omega_1{}^2$ is a constant for all experiments.

3.3.2. Water Suppression

Modern NMR pulse sequences suppress the water signal either by techniques that saturate or dephase the solvent magnetization or by techniques that return the solvent magnetization to the $+z$-axis prior to acquisition.[1] The pulse sequences used for $R_{1\rho}$ relaxation experiments shown in Figures 10, 12, and 13, with the exception of Figures 10d and 13a, use pulsed field gradients to dephase water magnetization. While these approaches provide high quality water suppression, sensitivity losses can result from saturation

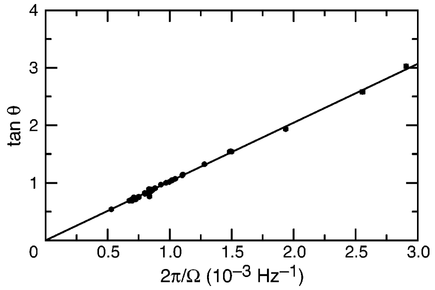

Figure 14. Calibration of ^{15}N field strengths using eq 54. The partially collapsed scalar coupling J_{eff} was measured from a ^{1}H−^{15}N HSQC experiment with off-resonance cw decoupling. The ^{15}N decoupling field was applied at 1000 Hz upfield of the center of the ^{15}N spectrum. Values of tan θ calculated from the ^{15}N resonances of ubiquitin are plotted as a function of $2\pi/\Omega$. A value of $\omega_1/2\pi = 1020 \pm 5$ Hz was obtained from a least-squares fit to the data.

transfer from the water ^{1}H spins. Incorporating water flip-back techniques into the sequence of Figure 10b, for example, particularly at high static magnetic field strengths, is infeasible because the 180° ^{1}H pulses applied during the ^{15}N spin-locking period invert the solvent magnetization and result in radiation damping. In contrast, modification of the pulse sequence shown in Figure 10c to incorporate water flip-back techniques may be possible because the 180° ^{1}H pulses during the relaxation delay are applied only when the S magnetization is stored on the z-axis. For example, the simple 180° ^{1}H pulses potentially could be replaced by soft 180°−hard 180° pulse sandwiches, in which the soft 180° pulse is water selective, to avoid exciting the water signal. The sequence shown in Figure 10d spin locks the water magnetization by the strong ^{1}H spin-lock rf field applied during the relaxation period. This simple approach allows the water magnetization to be returned to the $+z$-axis prior to acquisition, with the expected increase in sensitivity.[1] Although not yet demonstrated, similar approaches may allow water flip-back techniques to be incorporated into the ^{1}H$^{\mathrm{N}}$ pulse sequences of Figure 12. Any pulse sequence for measuring relaxation rate constants that incorporates water flip-back methods must be carefully validated to ensure that the initial state of the magnetization does not depend on the evolution of the water magnetization during the relaxation period T or T_{comp}.

3.3.3. Calibration of Radio Frequency Fields and Validation of Alignment

The amplitude of the ω_1 rf field is calibrated using off-resonance cw decoupling during either the indirect evolution or acquisition periods of either a one-dimensional or two-dimensional NMR experiment. The reduced scalar coupling constant is given by[5,50]

$$J_{\mathrm{eff}} = J_{IS} \cos\theta \tag{53}$$

The reference coupling is obtained from a control experiment performed without decoupling. This equation can be rearranged to yield

$$\tan\theta = [(J_{IS}/J_{\mathrm{eff}})^2 - 1]^{1/2} = \omega_1/\Omega \tag{54}$$

A plot of tan θ versus Ω^{-1} yields ω_1 as the slope of the resulting line. An example of the measurement is shown in Figure 14 for ^{15}N.

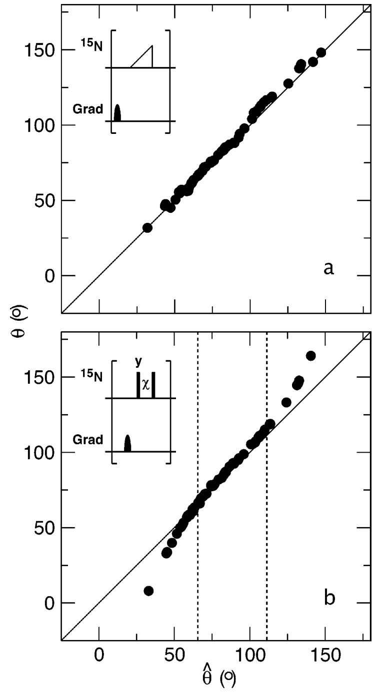

Figure 15. Alignment of magnetization in the tilted reference frame. Alignment was measured by incorporating the bracketed sequence elements shown in the insets into the pulse sequence of Figure 10a. In each experiment, two data sets were acquired in which the phase of the ^{15}N 90° pulse prior to the t_1 period in Figure 10a was inverted. Adding the two data sets yields signal intensities that are proportional to sin θ, and subtracting the two data sets yields signal intensities proportional to cos θ. The ordinate $\hat{\theta}$ is calculated for $\omega_1/2\pi = 500$ Hz. (a) A 4 ms adiabatic sweep with a tan/tanh profile[30] was used. (b) $\chi = 1/\omega_1 = 0.32$ ms. In (b), the dashed lines indicate the region between $\hat{\theta} = 68°$ and 112°.

Accurate alignment of magnetization along the direction of the effective field in the tilted reference frame is essential for optimal results. Components of the magnetization that are orthogonal to the effective field dephase rapidly due to $R_{2\rho}$ processes and the effects of B_1 inhomogeneity. This dephasing leads to an artifactual rapid initial decay of magnetization and reduces overall sensitivity. The accuracy of alignment obtained using either the adiabatic sweep of Figure 10b or the 90°−χ−90° pulse sequence element of Figure 10c can be evaluated by incorporating the pulse sequence elements shown in the insets to Figure 15 into the pulse sequence of Figure 10a. Examples of the quality of alignment obtained by these methods are shown in Figure 15. As expected from the above discussion, the adiabatic sweep is effective in obtaining alignment over the full ^{15}N spectral width, while the pulse technique achieves alignment for a spectral region of $-0.4\omega_1 < \Omega < +0.4\omega_1$.[8,30,32] However, the adiabatic sweep is ineffective at weak field strengths, $\omega_1/2\pi < 500$ Hz, because the duration of the sweep leads to significant relaxation losses.

4. Applications

Chemical exchange processes arise due to conformational transitions or chemical reactions on the chemical shift time scale that modify the magnetic environment of a given spin and consequently stochastically modulate its isotropic chemical shift. $R_{1\rho}$ spin relaxation in the rotating frame is one of a set of NMR techniques that can be used to characterize chemical exchange processes occurring on the microsecond

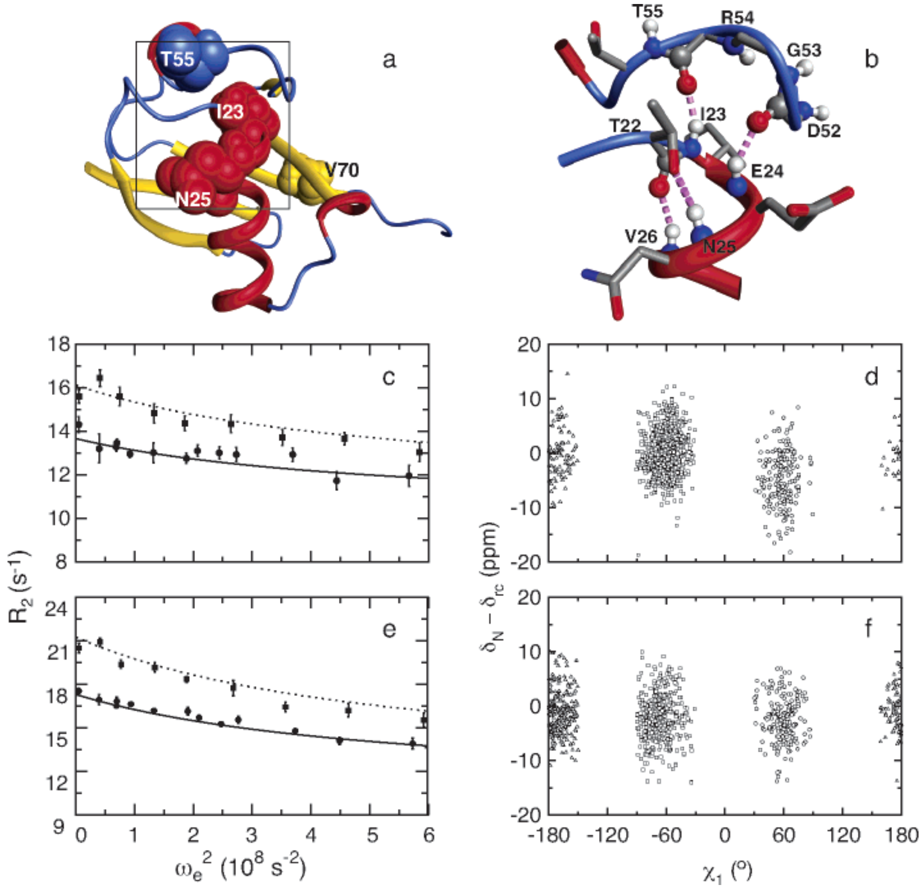

Figure 16. Ubiquitin ^{15}N $R_{1\rho}$relaxation dispersion.[53] (a) Ribbon representation of ubiquitin that shows the positions of the residues Ile 23, Asn 25, Thr 55, and Val 70 with exchange-broadened ^{15}N resonances. The boxed region is expanded in (b) to show hydrogen bonds (dashed lines) and side chain conformations. The transverse relaxation rate, R_2, is plotted as a function of the effective field, $\omega_e{}^2$, at $T = 280$ K for (c) Ile 23 and (e) Asn 25. Circles and squares represent data collected at magnetic fields of 11.7 and 14.1 T, respectively. Solid and dashed lines show the fitting of the data to a two-site fast exchange model, eq 30. R_2 data were obtained from $R_{1\rho}$ data using eq 20. R_1 was measured independently by conventional techniques.[73] The dependence of the ^{15}N chemical shift on the side chain angle χ_1 is shown for all (d) Ile and (f) Asn residues in the RefDB chemical shift database.[56] The structural representations in (a) and (b) were drawn using MOLMOL.[78]

to millisecond time scale.[2,5] In biological macromolecules, these processes often reflect time dependent phenomena that are critical to functions such as protein folding, ligand binding, and catalysis. Analysis of $R_{1\rho}$ relaxation dispersion data allows determination of the kinetic and thermodynamic properties of the conformational transitions or chemical reactions that give rise to exchange broadening and evaluation of the changes in isotropic shifts between the different molecular conformations or chemical species. $R_{1\rho}$ experiments have three principal advantages compared with other techniques, such as CPMG relaxation dispersion: (1) a wider range of effective fields in the rotating frame is accessible, allowing investigation of a large range of exchange rate constants, (2) combined variation of both ω_1 and ω_{rf} allows complete characterization of the exchange process using data recorded at single static magnetic field strengths, and (3) the absolute sign of chemical shift changes can be determined if exchange is outside the fast exchange limit.[9]

Values of isotropic chemical shift differences, $\Delta\omega_{ij}$, obtained from dispersion measurements contain structural information about normally unobservable minor molecular or chemical species. However, chemical shifts depend on multiple conformational parameters, such as backbone and side chain dihedral angles, electrostatic interactions, and hydrogen bonding.[51,52] Furthermore, a given conformational transition can affect the chemical shifts of different nuclei in different ways. These issues complicate the interpretation of chemical shift differences for any limited set of nuclear spins. Therefore, measurements of $R_{1\rho}$ dispersion data for multiple nuclei (for example, ^{15}N, ^{1}HN, ^{13}CO, and ^{13}C$^{\alpha}$ for the protein backbone) provide a more detailed picture of the exchange process.

As an example of ^{15}N $R_{1\rho}$ dispersion data and data analysis, Figure 16 shows the relaxation dispersion profile for residues Ile23 and Asn25 of ubiquitin at 280 K.[53] The dispersion data are described by a two-site fast exchange model, eq 30. The kinetic exchange rate constant, k_{ex}, is $\sim$25 000 s^{-1} for the backbone amide ^{15}N spins of residues Ile23, Asn25, Thr55, and Val70, suggesting that each spin is affected by the same conformational transition. Although p_1p_2 cannot be separated from $\Delta\omega_{21}$ in the limit of fast exchange, a model for the exchange process was proposed, based on calculation of chemical shifts[54,55] and analysis of a chemical shift database.[56] For example, Figure 16d shows that a change in the side chain dihedral angle χ_1 from $-60°$ to $+60°$ corresponds to an average upfield ^{15}N chemical shift of Ile of $\approx$4.5 ppm, while the ^{15}N shift of Asn is independent of χ_1, on average. The model suggests that the exchange process affecting residues Ile23, Asn25, and Thr55 is due to disruption of N-cap hydrogen bonds of the α-helix and repacking the side chain of Ile23. This mechanism is supported by the agreement between the calculated and measured ratios of $\Delta\omega_{21}{}^2$

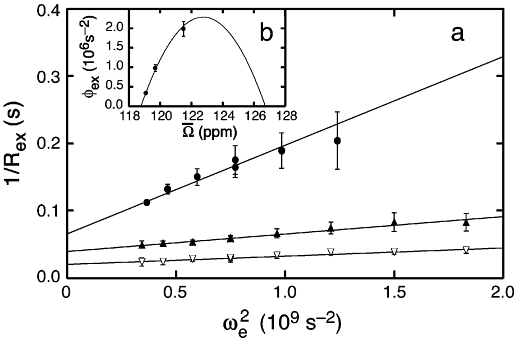

Figure 17. ^{15}N $R_{1\rho}$ relaxation dispersion profile for Ala11 of PSBD.[58] (a) Circles, filled triangles, and open triangles represent the data collected at 304, 313, and 323 K, respectively. R_{ex} rates were calculated from $R_{1\rho}$ rates using eq 21. $\bar{R}_1$ was measured independently by conventional techniques.[73] $\bar{R}_2$ was estimated from the relaxation interference rate constant as described elsewhere.[74,75] The solid lines represent the fit to eq 30. (b) $\phi_{ex} = p_1p_2\Delta\omega_{21}{}^2$ is plotted as a function of the isotropic chemical shift δ_N at each temperature. The solid line is the best fit to the function $\phi_{ex} = -\bar{\Omega}^2 + (\Omega_1 + \Omega_2)\bar{\Omega} - \Omega_1\Omega_2$. The x intercepts are $\Omega_1 = 118.80 \pm 0.02$ ppm and $\Omega_2 = 126.7 \pm 0.4$ ppm; thus, $\Delta\omega_{21} = 7.9 \pm 0.4$ ppm. The fitted value of Ω_2 is in good agreement with the predicted random coil chemical shift of 126 ppm.

for residues Ile23 and Thr55 and by amide proton solvent exchange protection factors.[57]

The following sections describe selected applications of $R_{1\rho}$ measurements to study protein and nucleic acid biological function and dynamics.

4.1. Protein Folding

$R_{1\rho}$ methods can characterize the kinetics of folding and can provide structural information concerning the ensemble of unfolded structures under equilibrium native state conditions, provided that the population of unfolded states is large enough to provide a broadening mechanism. Typically, the population of unfolded molecules must be approximately >0.005 for $R_{1\rho}$ experiments to be feasible. Folding studies that use a two-site model to fit relaxation dispersion data implicitly assume that kinetic transitions within the unfolded ensemble are fast.

A study of the peripheral subunit-binding domain (PSBD) of the dihydrolopoamide acetyltransferase component of the pyruvate dehydrogenase multienzyme complex from *Bacillus stearothermophilus* is the first example of ^{15}N $R_{1\rho}$ off-resonance relaxation measurements applied to protein folding.[58] Figure 17a shows relaxation dispersion curves for residue A11 at temperatures of 31, 40, and 50 °C. A fast exchange two-site model, eq 30, was used to fit the data. The temperature dependence of the exchange parameters was used to evaluate the independent values of p_1p_2 and $\Delta\omega_{21}$, that otherwise cannot be separately determined in the fast exchange limit, using the relationship $p_1p_2\Delta\omega_{21} = -\bar{\Omega}^2 + (\Omega_1 + \Omega_2)\bar{\Omega} - \Omega_1\Omega_2$, as shown in Figure 17b. The values of Ω_1 and Ω_2 obtained are consistent with a fully helical folded conformation and a fully random-coil unfolded conformation. The activation barriers for the folding and unfolding transitions were obtained from the temperature dependence of the folding and unfolding rate constants using the Arrhenius equation.

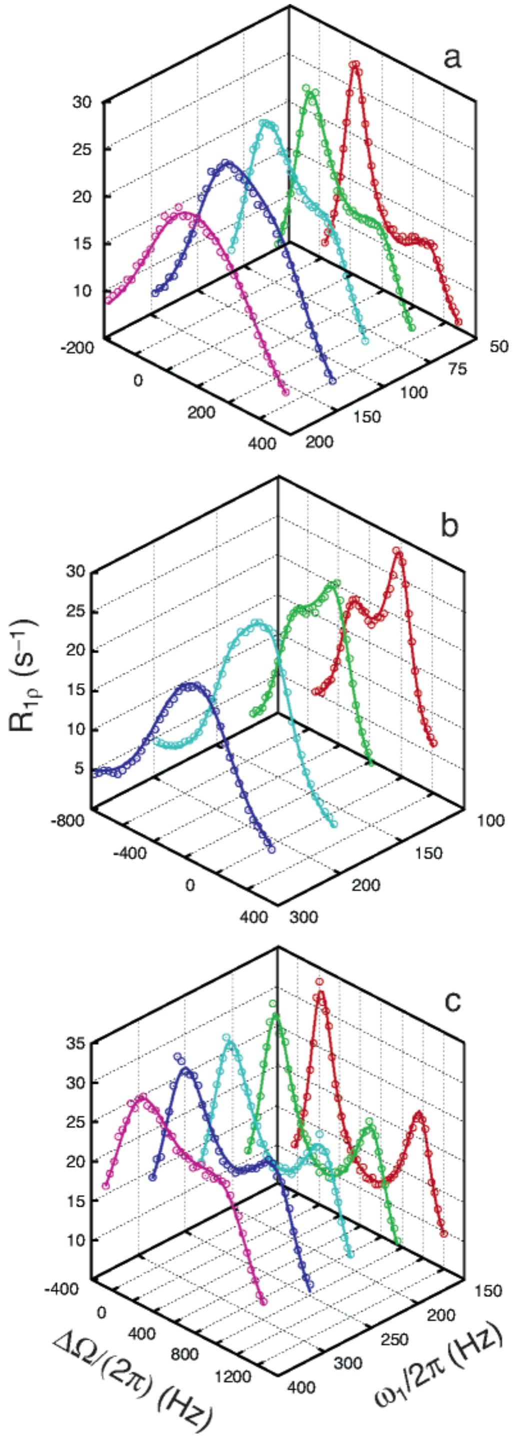

Figure 18. ^{15}N off-resonance $R_{1\rho}$ relaxation profiles for selected residues of the G48M Fyn SH3 domain. ^{15}N $R_{1\rho}$ data measured at a static magnetic field of 14.1 T, and best fit (solid) curves for residues (a) Thr14, (b) Glu11, and (c) Val55 are shown as a function of the spin-lock field strength, ω_1, and of the resonance offset from the spin-lock carrier, $\Delta\Omega$. The parameters obtained from the fits are as follows: $k_{ex} = 345 \pm 6$ s^{-1}, $p_2 = 0.0605 \pm 0.0009$, and $\Delta\omega_{21} = 4.30 \pm 0.01$ ppm for Thr14; $k_{ex} = 379 \pm 12$ s^{-1}, $p_2 = 0.0578 \pm 0.0016$, and $\Delta\omega_{21} = -5.78 \pm 0.01$ ppm for Glu11; $k_{ex} = 316 \pm 20$ s^{-1}, $p_2 = 0.0688 \pm 0.0044$, and $\Delta\omega_{21} = 16.21 \pm 0.02$ ppm for Val55. (Reprinted with permission from ref 7. Copyright 2005 American Chemical Society.)

In a recent study, ^{15}N off-resonance $R_{1\rho}$ relaxation rate constants were measured using spin-lock fields as low as 25 Hz to study folding of the Gly48Met mutant of the Fyn SH3 domain.[7] In this experiment, the $R_{1\rho}$ relaxation rate constant for a single residue is measured using a one-dimensional NMR experiment with selective Hartmann−Hahn polarization transfer (Figure 10d). Figure 18 shows the relaxation dispersion profiles for residues Thr14, Glu11,

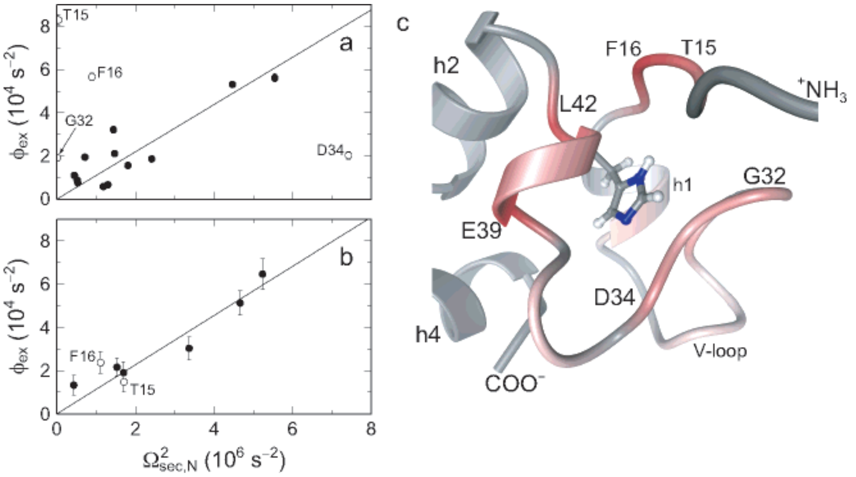

Figure 19. Structural interpretation of chemical exchange line broadening in HP67. (a) ϕ_{ex} values of WT HP67 are plotted versus the square of the ^{15}N secondary chemical shift, $\Omega_{sec,N}{}^2$. The secondary shift $\Omega_{sec,N} = \Omega_{rc} - \Omega_0$, where Ω_{rc} is the random coil chemical shift expected for an unfolded conformation and Ω_0 is the chemical shift observed in the native state. The straight line corresponds to the weighted least-squares slope of $p_1p_2 = (1.10 \pm 0.09) \times 10^{-2}$, with a correlation coefficient $r = 0.90$. Residues represented with open symbols have been excluded from the analysis and maintain residual interactions with the His41 in the WT protein. (b) ϕ_{ex} values of His41Tyr HP67 are plotted versus the square of the ^{15}N secondary chemical shift, $\Omega_{sec,N}{}^2$. The straight line corresponds to the weighted least-squares slope of $p_1p_2 = (1.14 \pm 0.07) \times 10^{-2}$, with a correlation coefficient $r = 0.94$. Residues represented with open symbols maintained residual interactions with the His41 in the WT protein that are absent in the His41Tyr HP67 mutant protein. (c) The combined deviation of amide ^{1}H and ^{15}N chemical shift changes from the secondary chemical shift, $\Omega_{sec,H}$ and $\Omega_{sec,N}$, $[(\Delta\omega_H - \Omega_{sec,H})^2 + (\Delta\omega_N - \Omega_{sec,N})^2]^{1/2}$, in units of angular frequency for a static magnetic field strength of 11.7T, is mapped onto the structure of HP67; the color is interpolated between white (0 s^{-1}) and red ($\geq$3000 s^{-1}). Residues for which data are not available are represented in gray. The structural representation was drawn using MOLMOL.[78]

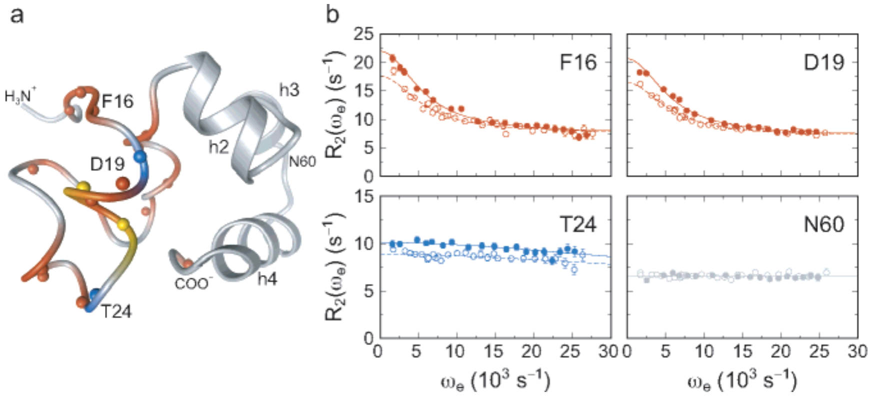

Figure 20. Chemical exchange in WT HP67 at pH 7.0 and 293 K. (a) Residue-specific exchange model selection for the analysis of ^{15}N $R_{1\rho}$ relaxation data is highlighted on the structure of HP67. The spheres represent the backbone nitrogen atoms. The different exchange models are represented with different colors: absence of relaxation (gray), two-state fast chemical exchange (orange, $k_{ex} = (5.7 \pm 0.1) \times 10^3$ s^{-1}, and blue, $k_{ex} = (4.2 \pm 0.5) \times 10^4$ s^{-1}), and three-state fast chemical exchange (yellow). (b) Representative ^{15}N $R_2(\omega_e)$ relaxation dispersion profiles measured at static magnetic field strengths of 11.7 T (open symbols) and 14.1 T (closed symbols) are shown for Phe16, Asp19, Thr24, and Asn60. The best fits of the experimental data obtained from the global analysis of the relaxation dispersion data for all exchanging residues at both static magnetic field strengths are shown as solid and dashed lines for 14.1 and 11.7 T, respectively. The structural representation was drawn using MOLMOL.[78]

and Val55. The two-site exchange process is accurately characterized using the dispersion profiles collected at one static magnetic field strength and a spin-lock field strength of the same order of magnitude as the exchange rate constant. The same system has previously been characterized extensively using CPMG relaxation dispersion using three static magnetic field strengths.[59] A significant advantage of the $R_{1\rho}$ approach, compared to CPMG techniques, is that complete characterization is possible using only a single static magnetic field strength.

A partially folded intermediate of the villin headpiece N-terminal domain (HP67) was very recently characterized using a combination of ^{15}N on- and off-resonance $R_{1\rho}$ and CPMG relaxation measurements.[60] This intermediate, characterized by an unfolded N-terminal subdomain and a folded C-terminal subdomain, is at equilibrium with the native state. At neutral pH and at 293 K the forward and reverse rate constants are equal to 60 and 5600 s^{-1}, respectively. The comparative study of the wild-type (WT) and the His41Tyr mutant HP67 indicates that, in the partially folded intermediate, the majority of the residues in the N-terminal region sample random-coil conformations, while some residues maintain residual interactions with the His41 in the WT protein that are absent in the mutant protein (see Figure 19). These results suggest that the partially folded intermediate contains a relatively stable core around His41. The ^{15}N $R_{1\rho}$ relaxation dispersion data of all the residues in HP67 are analyzed using four exchange models: absence of chemical exchange broadening, two-state fast chemical exchange, two-state chemical exchange not constrained to be fast on the chemical shift time scale, and three-state fast chemical exchange. The rules for the selection of a particular chemical

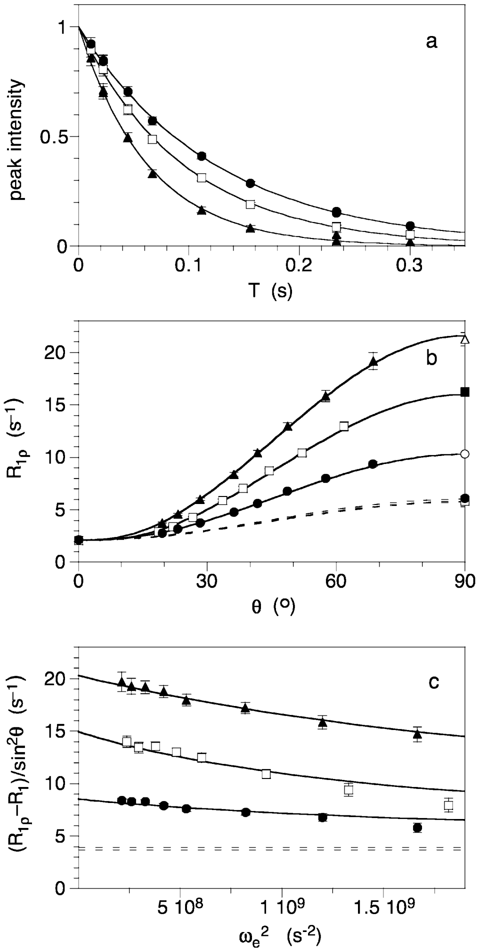

Figure 21. Off-resonance ^{15}N $R_{1\rho}$ relaxation for the Glu140Gln mutant of the camodulin C-terminal domain, Tr$_2$C. Relaxation dispersion data are represented for the residues (filled circles) Arg86, (filled triangles) Ser101, and (open squares) Asp131. (a) Relaxation decay curves and exponential fit $I(t) = I(0)\exp(-R_{1\rho}T)$, obtained at $\theta = 57.5°$ with $R_{1\rho} = 8.0 \pm 0.2$ s^{-1} for Arg86, obtained at $\theta = 57.5°$ with $R_{1\rho} = 15.8 \pm 0.5$ s^{-1} for Ser101, and obtained at $\theta = 52.1°$ with $R_{1\rho} = 10.4 \pm 0.2$ s^{-1} for Asp131. (b) $R_{1\rho}$ rate constants are plotted as a function of the tilt angle, θ. (c) $R_{1\rho}$ rate constants are plotted as a function of the effective field, ω_e^2. The solid lines show the fit to a two-site fast exchange model. The dashed lines show the profiles expected in the absence of chemical exchange. In the fits, the four parameters $\bar{R}_1$, $\bar{R}_2$, τ_{ex}, and ϕ_{ex} are simultaneously optimized for each ^{15}N spin. The optimized values of k_{ex}, ϕ_{ex} are 49 300 ± 5000 s^{-1}, (269 ± 27) × 10^3 s^{-2} for Arg86, 59 000 ± 6000 s^{-1}, (980 ± 104) × 10^3 s^{-2} for Ser101, and 43000 ± 3000 s^{-1}, (484 ± 36) × 10^3 s^{-2} for Asp131. (Reprinted from ref 64, Copyright 2001, with permission from Elsevier.)

exchange model are explained in detail in this study.[60] Figure 20 illustrates the models selected for the analysis of the ^{15}N $R_{1\rho}$ relaxation dispersion data of the different residues of HP67. The dispersion data for residues that yielded similar values of k_{ex} are globally fitted to obtain a single global value of k_{ex} and residue-specific values of $\bar{R}_1$, $\bar{R}_2$, and ϕ_{ex}.

4.2. Ligand Binding

Conformational dynamics are important in recognition of one or more binding partners by proteins and other macromolecules, such as RNA/DNA aptamers. A macromolecule in solution samples an ensemble of different states. A ligand might either select among preexisting states that are capable of binding[61−64] or induce a transition to a state that is capable of binding.[65] These two mechanisms are referred to as "selected-fit" or "induced-fit", respectively. In either case, the interchange between competent and incompetent states, relative to binding, can be measured with $R_{1\rho}$ relaxation methods.

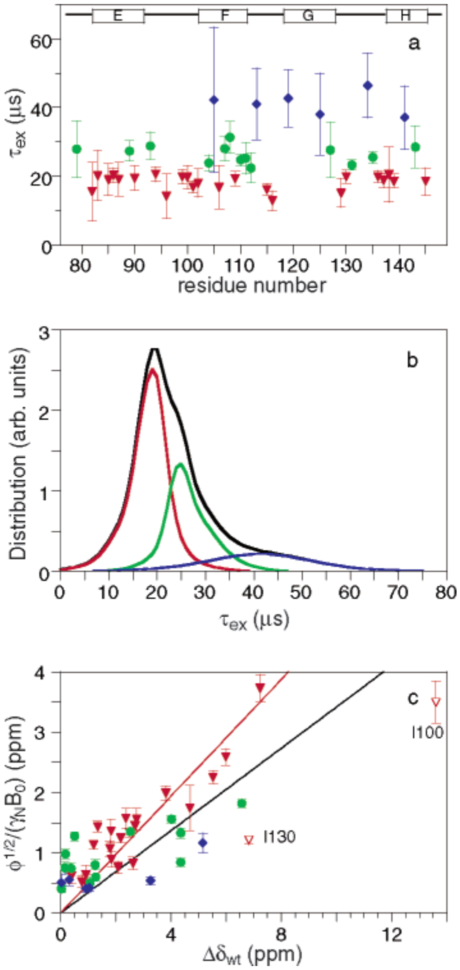

Figure 22. Chemical exchange correlation time, $\tau_{ex} = 1/k_{ex}$. Three different groups of residues have been identified using cluster analysis of the values of k_{ex}: red triangles, k_{ex} = 54 100 ± 7100 s^{-1}; green circles, k_{ex} = 39 700 ± 4200 s^{-1}; and blue diamonds, k_{ex} = 24 300 ± 6000 s^{-1}. (a) τ_{ex} is presented as a function of the amino acid sequence. (b) The distribution of τ_{ex} values is shown for the three groups. (c) ϕ_{ex} values of (Ca^{2+})$_2$-Glu140Gln Tr$_2$C are compared to the Ca^{2+} induced ^{15}N chemical shift changes in wild-type Tr$_2$C; the same color coding applies. (Reprinted from ref 64, Copyright 2001, with permission from Elsevier.)

$R_{1\rho}$ relaxation experiments for ^{15}N, ^{1}H^N, ^{13}CO, and ^{13}C$^\alpha$ have been used to characterize the transition between open and closed states of the Ca^{2+}-loaded state of the Glu140Gln mutant of the calmodulin C-terminal domain.[15,16,40,64] Figure 21 shows ^{15}N relaxation dispersion data for residues Arg86, Ser101, and Asp131. The data were fit to a two-site fast exchange model, eq 30. Analysis of the exchange rates indicated that the residues are clustered in three groups, as shown in Figure 22b. Correlation of the ^{15}N chemical shift difference between the apo and (Ca^{2+})$_2$ states and the measured values of $p_1p_2\Delta\omega_{21}$ allowed the evaluation of the equilibrium populations of the two states, as shown in Figure 22c, yielding $p_2 = 0.50 \pm 0.17$. The kinetic rate constants measured for the different nuclear species are in good agreement: the weighted average values of k_{ex} are 47 600 ± 6800 s^{-1}, 52 600 ± 19 400 s^{-1}, and 40 000 ± 12 800 s^{-1} for ^{15}N, ^{1}H, and ^{13}C$^\alpha$, respectively. Suprisingly, the chemical shift differences for ^{13}C$^\alpha$ are not correlated with the chemical

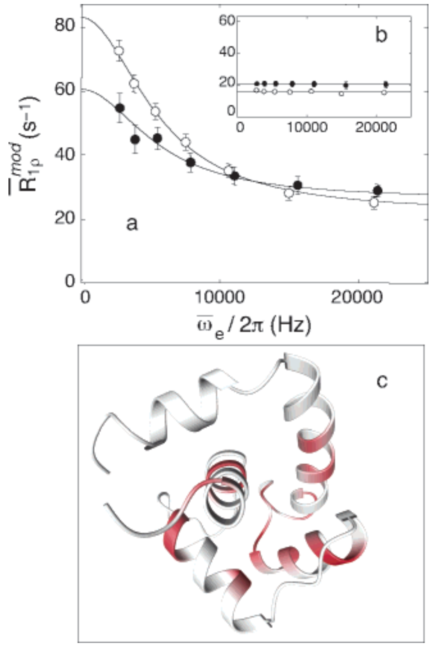

Figure 23. $^1H^N$ relaxation dispersion profile of the Ca^{2+}-loaded regulatory domain of the cardiac troponin C (Ca^{2+}-NcTnC) at a static magnetic field strength of 600 (filled circles) and 800 (open circles) MHz at $T = 286$ K. $\bar{R}_{1\rho}^{\mathrm{mod}}$ and $\bar{\omega}_e$ are determined from two experiments acquired with the rf carrier positioned symmetrically upfield and downfield of the center of the $^1H^N$ spectral region, as described elsewhere.[17] Relaxation dispersion curves are shown for residues Leu 41 (a) and Ala 22 (b); the latter does not show detectable dispersion and serves as a control. (a) The solid curves show the best fit to a two-site fast exchange model, with $k_{ex} = 34\,700 \pm 6000$ s^{-1} and $p_1p_2\Delta\omega_{21}{}^2 = (1.19 \pm 0.14) \times 10^6$ s^{-2} (at 14.1 T) for Leu 41. (c) Ribbon representation of Ca^{2+}-NcTnC. Residues are color coded according to the value of $1/k_{ex}$ from white (0) to red (40 μs). The structural representation was drawn using MOLMOL.[78] (Reprinted Figure 5 from ref 17 with kind permission of Springer Science and Business Media. Copyright 2005.)

shift difference between the apo and (Ca^{2+})$_2$ states. This observation suggests that the conformational transition is more complex than anticipated solely from the ^{15}N results. The exchange rate constants match the estimated Ca^{2+} off-rate, indicating that Ca^{2+} release may be gated by the conformational transition.

The transition between open and closed conformations of the Ca^{2+}-loaded regulatory domain of the cardiac troponin C has been studied using the $^1H^N$ $R_{1\rho}$ relaxation experiment presented in Figure 12c.[17] Figure 23a and b depicts the $^1H^N$ relaxation dispersion curves of two representative residues. The flat profile shown in Figure 23b is a control indicating that artifact-free data are obtained for residues not subject to exchange. The exchange rate constant calculated from the fit of 16 of the 20 residues that show relaxation dispersion is $\sim$35 000 s^{-1}, indicative of a concerted motion of the residues. These residues are located at the hinge regions and in the so-called defunct Ca^{2+}-binding site as shown in Figure 23c. The range of effective fields used in this experiment is very large, which allows extensive sampling of the dispersion curve and studies of motions characterized by time scales shorter than 100 μs.

4.3. Catalysis

Conformational transitions needed to open/close the active site or to position key functional groups during enzyme catalysis may be rate limiting.[66−69] Elucidation of such conformational processes is of great importance for a molecular understanding of enzyme catalysis. Use of substrate analogues, transition state mimics, and inhibitors can help identify the distinct contributions of the enzyme dynamics at different stages of the catalytic process, as the reaction coordinate evolves from substrate binding to catalysis to product release.[66,68] In addition, for some reversible enzymes, chemical exchange broadening can be measured under conditions in which the enzyme is actively turning over substrate.[70]

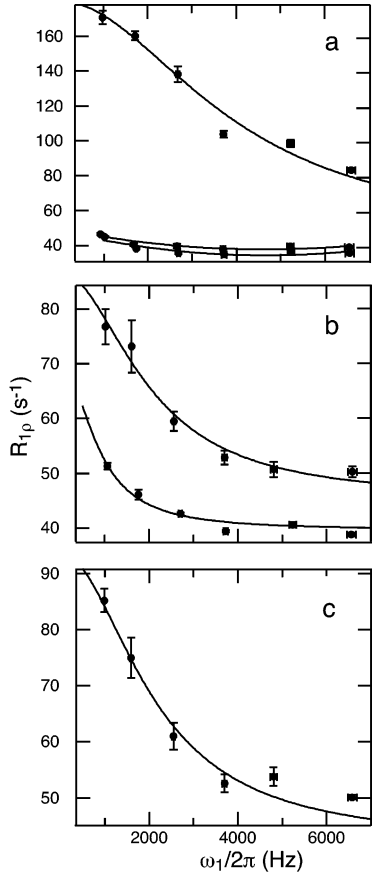

Figure 24. $R_{1\rho}$ relaxation dispersion for the lead-dependent ribozyme. The spectra were collected at $T = 298$ K and at a static magnetic field of 11.7 T. (a) Relaxation dispersion curves are shown for A25 C2 (upper curve) and A12 C2 and A8 C2 (lower curves). (b) Relaxation dispersion curves for A18 C8 (upper curve) and A18 C2 (lower curve). (c) Relaxation dispersion curve for G7 C8. Solid curves are the fits to a two-site fast exchange model, except for the two lower curves in (a), which are third-degree polynomials. Estimated values of k_{ex} are 13 000 ± 2000 s^{-1} for G7 C8, 13 000 ± 3000 s^{-1} for A18 C8, 5300 ± 4600 s^{-1} for A18 C2, and 25 000 ± 1000 s^{-1} for A25 C2. (Reprinted with permission from ref 28. Copyright 2000 American Chemical Society.)

Apo and inhibitor-bound forms of HIV-1 protease have been studied using ^{15}N and $^1H^N$ $R_{1\rho}$ relaxation experiments.[14,71] In these studies, chemical exchange processes occurring in two different regions of the enzyme are identified. The flaps that cover the active site in the inhibitor-bound form exhibit a conformational transition on the 100 μs time scale in the apo state. On the other hand, residues at the dimer interface are mobile on the millisecond time scale. Even in the fast exchange limit, the ratio of the chemical shift difference $\Delta\omega_{21}^{H}/\Delta\omega_{21}^{N} = (\phi_{ex}^{H}/\phi_{ex}^{N})^{1/2}$, obtained from $^1H^N$ and ^{15}N $R_{1\rho}$ relaxation dispersion measurements, provides qualitative structural information on the types of conformational transitions determining the exchange process.

A smaller number of applications of $R_{1\rho}$ relaxation dispersion measurements for nucleic acids have been reported.[28,29] The conformational dynamics of the lead-dependent ribozyme has been investigated using ^{13}C $R_{1\rho}$ relaxation experiments.[28] Residues in the active site present conformational dynamics with an exchange rate constant in the range 5000−25 000 s^{-1}, as shown in Figure 24. Residues in the GAAA tetraloop loop motif are also flexible, suggesting the presence of a dynamic network of stabilizing H-bonds. This study emphasizes the importance of dynamics in the catalytic function of RNA molecules.

5. Conclusions

Although line shape analysis and CPMG relaxation dispersion have been more commonly utilized than $R_{1\rho}$ relaxation dispersion, recent theoretical and experimental advances have made $R_{1\rho}$ measurements much more powerful for characterizing microsecond to millisecond conformational dynamics and chemical kinetics in proteins and other biomacromolecules. The number of applications that use $R_{1\rho}$ techniques is increasing, and new insights are already emerging about dynamic events in folding, recognition, and catalysis. Most importantly, new experimental techniques allow measurements to be made over a very wide range of resonance offsets and effective fields in the rotating frame to take advantage of new theoretical descriptions relating $R_{1\rho}$ to two-site and *N*-site exchange processes that are not in the fast-exchange limit. The combination of these developments opens exciting new vistas for experimental investigations of the linkage between structure and dynamics in the function of biomacromolecules.

6. Acknowledgments

Support from National Institutes of Health Grant GM59273 (A.G.P.) is gratefully acknowledged. We thank Michael J. Grey (Columbia University) for providing Figure 11 and the cover illustration and Nikolai R. Skrynnikov (Purdue University) for providing Figure 23 in advance of publication.

7. References

(1) Cavanagh, J.; Fairbrother, W. J.; Palmer, A. G.; Skelton, N. J. *Protein NMR Spectroscopy: Principles and practice*; Academic Press: San Diego, CA, 1996.
(2) Palmer, A. G. *Chem. Rev.* **2004**, *104*, 3623.
(3) Igumenova, T. I.; Wand, A. J. *Chem. Rev.* **2006**, *106*, http://dx.doi.org/10.1021/cr040422h.
(4) Goehlert, V. A.; Stone, M. J. *Chem. Rev.* **2006**, *106*, http://dx.doi.org/10.1021/cr040421p.
(5) Palmer, A. G.; Kroenke, C. D.; Loria, J. P. *Methods Enzymol.* **2001**, *339*, 204.
(6) Fischer, M. W. F.; Majumdar, A.; Zuiderweg, E. R. P. *Prog. Nucl. Magn. Reson. Spectrosc.* **1998**, *33*, 207.
(7) Korzhnev, D. M.; Orekhov, V. Y.; Kay, L. E. *J. Am. Chem. Soc.* **2005**, *127*, 713.
(8) Massi, F.; Johnson, E.; Wang, C.; Rance, M.; Palmer, A. G. *J. Am. Chem. Soc.* **2004**, *126*, 2247.
(9) Trott, O.; Palmer, A. G. *J. Magn. Reson.* **2002**, *154*, 157.
(10) Trott, O.; Abergel, D.; Palmer, A. G. *Mol. Phys.* **2003**, *101*, 753.
(11) Trott, O.; Palmer, A. G. *J. Magn. Reson.* **2004**, *170*, 104.
(12) Abergel, D.; Palmer, A. G. *Concepts Magn. Reson., A* **2003**, *19*, 134.
(13) Korzhnev, D. M.; Skrynnikov, N. S.; Millet, O.; Torchia, D. A.; Kay, L. E. *J. Am. Chem. Soc.* **2002**, *124*, 10743.
(14) Ishima, R.; Wingfield, P. T.; Stahl, S. J.; Kaufman, J. D.; Torchia, D. A. *J. Am. Chem. Soc.* **1998**, *120*, 10534.
(15) Mulder, F. A. A.; Akke, M. *Magn. Reson. Chem.* **2003**, *41*, 853.
(16) Lundstrom, P.; Akke, M. *ChemBioChem* **2005**, *6*, 1685.
(17) Eichmuller, C.; Skrynnikov, N. R. *J. Biomol. NMR* **2005**, *32*, 281.
(18) Abragam, A. *Principles of Nuclear Magnetism*; Clarendon Press: Oxford, U.K., 1961.
(19) Abergel, D.; Palmer, A. G. *J. Phys. Chem. B* **2005**, *109*, 4837.
(20) McConnell, H. M. *J. Chem. Phys.* **1958**, *28*, 430.
(21) Ernst, R. R.; Bodenhausen, G.; Wokaun, A. *Principles of nuclear magnetic resonance in one and two dimensions*; Oxford University Press: Oxford, U.K., 1987.
(22) Ishima, R.; Torchia, D. A. *J. Biomol. NMR*, in press.
(23) Desvaux, H.; Berthault, P. *Prog. Nucl. Magn. Reson. Spectrosc.* **1999**, *35*, 295.
(24) Wennerström, H. *Mol. Phys.* **1972**, *24*, 69.
(25) Abergel, D.; Palmer, A. G. *ChemPhysChem* **2004**, *5*, 787.
(26) Miloushev, V. Z.; Palmer, A. G. *J. Magn. Reson.* **2005**, *177*, 221.
(27) Michaeli, S.; Sorce, D. J.; Idiyatullin, D.; Ugurbil, K.; Garwood, M. *J. Magn. Reson.* **2004**, *169*, 293.
(28) Hoogstraten, C. G.; Wank, J. R.; Pardi, A. *Biochemistry* **2000**, *39*, 9951.
(29) Maltseva, T. V.; Foldesi, A.; Ossipov, D.; Chattopadhyaya, J. *Magn. Reson. Chem.* **2000**, *38*, 403.
(30) Mulder, F. A. A.; de Graaf, R. A.; Kaptein, R.; Boelens, R. *J. Magn. Reson.* **1998**, *131*, 351.
(31) Akke, M.; Palmer, A. G. *J. Am. Chem. Soc.* **1996**, *118*, 911.
(32) Kim, S.; Baum, J. *J. Biomol. NMR* **2004**, *30*, 195.
(33) Kempf, J. G.; Jung, J. Y.; Sampson, N. S.; Loria, J. P. *J. Am. Chem. Soc.* **2003**, *125*, 12064.
(34) Pervushin, K.; Riek, R.; Wider, G.; Wüthrich, K. *Proc. Natl. Acad. Sci. U.S.A.* **1997**, *94*, 12366.
(35) Pelupessy, P.; Chiarparin, E.; Bodenhausen, G. *J. Magn. Reson.* **1999**, *1138*, 178.
(36) Pelupessy, P.; Chiarparin, E. *Concepts Magn. Reson.* **2000**, *12*, 103.
(37) Yamazaki, T.; Muhandiram, R.; Kay, L. E. *J. Am. Chem. Soc.* **1994**, *116*, 8266.
(38) Abramowitz, M.; Stegun, I. A. *Handbook of mathematical functions with formulas, graphs, and mathematical tables*; Dover Publications: New York, 1974.
(39) Grey, M. J.; Wang, C.; Palmer, A. G. *J. Am. Chem. Soc.* **2003**, *125*, 14324.
(40) Lundstrom, P.; Akke, M. *J. Biomol. NMR* **2005**, *32*, 163.
(41) Ulmer, T. S.; Campbell, I. D.; Boyd, J. *J. Magn. Reson.* **2004**, *166*, 190.
(42) Wand, A. J.; Bieber, R. J.; Urbauer, J. L.; McEvoy, R. P.; Gan, Z. *J. Magn. Reson., Ser. B* **1995**, *108*, 173.
(43) Kushlan, D. M.; LeMaster, D. M. *J. Am. Chem. Soc.* **1993**, *115*, 11026.
(44) Palmer, A. G.; Cavanagh, J.; Wright, P. E.; Rance, M. *J. Magn. Reson.* **1991**, *93*, 151.
(45) Kay, L. E.; Keifer, P.; Saarinen, T. *J. Am. Chem. Soc.* **1992**, *114*, 10663.
(46) Desvaux, H.; Birlirakis, N.; Wary, C.; Berthault, P. *Mol. Phys.* **1995**, *86*, 1059.
(47) Desvaux, H.; Goldman, M. *J. Magn. Reson., Ser. B* **1996**, *110*, 198.
(48) Schleucher, J.; Quant, J.; Glaser, S. J.; Griesinger, C. *J. Magn. Reson., Ser. A* **1995**, *112*, 144.
(49) Wang, A. C.; Bax, A. *J. Biomol. NMR* **1993**, *3*, 715.
(50) Shaka, A. J.; Keeler, J. *Prog. Nucl. Magn. Reson. Spectrosc.* **1987**, *19*, 47.
(51) Wishart, D. S.; Case, D. A. *Methods Enzymol.* **2001**, *338*, 3.
(52) de Dios, A. C.; Pearson, J. G.; Oldfield, E. *Science* **1993**, *260*, 1491.
(53) Massi, F.; Grey, M. J.; Palmer, A. G. *Protein Sci.* **2005**, *14*, 735.
(54) Xu, X. P.; Case, D. A. *J. Biomol. NMR* **2001**, *21*, 321.
(55) Xu, X. P.; Case, D. A. *Biopolymers* **2002**, *65*, 408.
(56) Zhang, H.; Neal, S.; Wishart, D. S. *J. Biomol. NMR* **2003**, *25*, 173.
(57) Cordier, F.; Grzesiek, S. *J. Mol. Biol.* **2002**, *317*, 739.
(58) Vugmeyster, L.; Kroenke, C. D.; Picart, F.; Palmer, A. G.; Raleigh, D. P. *J. Am. Chem. Soc.* **2000**, *122*, 5387.
(59) Korzhnev, D. M.; Salvatella, X.; M, M. V.; Nardo, A. A. D.; Davidson, A. R.; Dobson, C. M.; Kay, L. E. *Nature* **2004**, *430*, 586.
(60) Grey, M. J.; Tang, Y.; Alexov, E.; McKnight, C. J.; Raleigh, D. P.; Palmer, A. G. *J. Mol. Biol.* **2006**, *355*, 1078.
(61) Volkman, B. F.; Lipson, D.; Wemmer, D. E.; Kern, D. *Science* **2001**, *291*, 2429.
(62) Wang, C.; Karpowich, N.; Hunt, J. F.; Rance, M.; Palmer, A. G. *J. Mol. Biol.* **2004**, *342*, 525.
(63) Feher, V. A.; Cavanagh, J. *Nature* **1999**, *400*, 289.
(64) Evenäs, J.; Malmendal, A.; Akke, M. *Structure* **2001**, *9*, 185.
(65) James, L. C.; Tawfik, D. S. *Trends Biochem. Sci.* **2003**, *28*, 361.
(66) Kovrigin, E. L.; Cole, R.; Loria, J. P. *Biochemistry* **2003**, *42*, 5279.
(67) Wolf-Watz, M.; Thai, V.; Henzler-Wildman, K.; Hadjipavlou, G.; Eisenmesser, E. Z.; Kern, D. *Nat. Struct. Biol.* **2004**, *11*, 945.
(68) Rozovsky, S.; McDermott, A. E. *J. Mol. Biol.* **2001**, *310*, 259.
(69) Butterwick, J. A.; Loria, J. P.; Astrof, N. S.; Kroenke, C. D.; Cole, R.; Rance, M.; Palmer, A. G. *J. Mol. Biol.* **2004**, *339*, 855.
(70) Eisenmesser, E. Z.; Bosco, D. A.; Akke, M.; Kern, D. *Science* **2002**, *295*, 1520.

(71) Ishima, R.; Freedberg, D.; Wang, Y.-X.; Louis, J. M.; Torchia, D. A. *Structure* **1999**, *7*, 1047.
(72) Shaka, A. J.; Barker, P. B.; Freeman, R. *J. Magn. Reson.* **1985**, *64*, 547.
(73) Farrow, N. A.; Muhandiram, R.; Singer, A. U.; Pascal, S. M.; Kay, C. M.; Gish, G.; Shoelson, S. E.; Pawson, T.; Forman-Kay, J. D.; Kay, L. E. *Biochemistry* **1994**, *33*, 5984.
(74) Kroenke, C. D.; Loria, J. P.; Lee, L. K.; Rance, M.; Palmer, A. G. *J. Am. Chem. Soc.* **1998**, *120*, 7905.
(75) Wang, C.; Grey, M. J.; Palmer, A. G. *J. Biomol. NMR* **2001**, *21*, 361.
(76) Marion, D.; Ikura, M.; Tschudin, R.; Bax, A. *J. Magn. Reson.* **1989**, *85*, 393.
(77) Shaka, A. J.; Keeler, J.; Frenkiel, T.; Freeman, R. *J. Magn. Reson.* **1983**, *52*, 334.
(78) Koradi, R.; Billeter, M.; Wüthrich, K. *J. Mol. Graph.* **1996**, *14*, 51.

CR0404287